Mathematics and Computers in Simulation xxx (xxxx) xxx

Contents lists available at ScienceDirect

Mathematics and Computers in Simulation

journal homepage: www.elsevier.com/locate/matcom

Original articles

Numerical adiabatic perturbation theory for the absolute $|K|(p, p)$ equation

Rubén Garralon-López, Francisco Rus, Francisco R. Villatoro *

Escuela de Ingenierías Industriales, Dept. de Lenguajes y Ciencias de la Computación, Universidad de Málaga, 29071, Málaga, Spain

ARTICLE INFO

Keywords:
Compactons
Nonlinear dispersion
Numerical simulation
Numerically-induced phenomena
Adiabatic perturbation theory

ABSTRACT

In physical applications, the absolute $|K|(p, p)$ equation should be preferred to the widely used Rosenau–Hyman $K(p, p)$ equation due to the robustness of its compactons and anticompactons interactions observed in numerical simulations with small hyperviscosity. In order to understand the effect of the hyperviscosity in solutions with multiple compactons of the $|K|(p, p)$ equation, the adiabatic perturbation theory has been applied. For a single compacton, this theory can be solved analytically showing that the second invariant decreases for p smaller than a critical value, as expected for a dissipative perturbation, but increases otherwise. This analytical prediction is in good agreement with the numerical results. In order to predict the evolution of the second invariant in time as a function of the hyperviscosity parameter for general solutions of the $K(p, p)$ equation, a numerical implementation of the adiabatic perturbation theory has been developed. This adiabatic numerical prediction agrees with the evolution of the second invariant in the propagation of a single compacton, the generation of compacton trains from a truncated cosine initial condition, and compacton–compacton chase collisions. However, discrepancies emerge in other scenarios, such as the generation of a compacton train from a dilated compacton and in compacton–anticompacton chase collisions. Our findings support the use of the numerical adiabatic perturbation theory for analyzing the evolution of invariants due to hyperviscosity in multi-compacton simulations.

1. Introduction

Compactons and anticompactons are compactly supported solitary waves discovered by Rosenau and Hyman in the so-called $K(p, p)$ equation [31,32]. They are a manifestation of the balance between nonlinear inertia and nonlinear dispersion, where the nonlinearity enhances or weakens the inertial or dispersive forces. These phenomena can be modeled by power laws with non-integer exponents fitted from experimental data; the standard fit with the power law u^p can be used only when $u > 0$, since it is complex-valued where $u < 0$ for non-integer p. A physical example is the flow in deformable porous media, where the constitutive equation for the permeability is a power law of the porosity (the volume fraction occupied by the melt) [38]; an specific application is the magma flow through a viscous matrix composed of incompressible solid grains [42]. Moreover, it is necessary that the resulting evolution equation preserves the positivity of the initial condition to avoid complex values in some regions of the domain; in fact, numerical simulations of the $K(p, p)$ equation have shown that solutions with multiple compactons in interaction generate ripples with non-positive parts [7,11,34,43]. For real-valued solutions, the power-law should be substituted by the even function $|u|^p$, or the odd function $|u|^{p-1}\,u$, depending on the specific application. In the last case, the resulting physical model is the so-called absolute

* Corresponding author.
E-mail addresses: rubengarralon7@uma.es (R. Garralon-López), fdrus@uma.es (F. Rus), frvillatoro@uma.es (F.R. Villatoro).

https://doi.org/10.1016/j.matcom.2024.03.031
Received 25 August 2023; Received in revised form 11 January 2024; Accepted 25 March 2024
Available online 28 March 2024

Please cite this article as: Rubén Garralon-López et al., *Mathematics and Computers in Simulation*, https://doi.org/10.1016/j.matcom.2024.03.031

Rosenau–Hyman $|K|(p,p)$ equation [13,14], given by

$$u_t + (|u|^{p-1}\,u)_x + (|u|^{p-1}\,u)_{xxx} = 0, \tag{1}$$

where u is the amplitude, x is space, t is time, subindexes indicate differentiation, and $p > 1$. It was briefly discussed and named signed $K(p,p)$ equation by Galaktionov and Svirshchevskii [9]; moreover, the $|K|(p,1)$ equation was referred to as modular Korteweg–de Vries equation by Pelinovsky et al. [26,37]. There is an additional advantage of the $|K|(p,p)$ equation with respect to the $K(p,p)$ when p is an even integer and u can be negative: in computer simulations, the collisions between compactons and anticompactons of large amplitude blow up for even p; however, the corresponding solutions for the $|K|(p,p)$ are stable and robust [14,26].

The study of compacton and anticompacton chase collisions, and the generation of compacton trains from arbitrary initial conditions for the $|K|(p,p)$ equation require the use of numerical methods. We have used a Petrov–Galerkin numerical method with hyperviscosity for this equation [13,14]. However, any numerical method for the $K(p,p)$ equation could also be used: pseudospectral in space and variable order, variable timestep Adams–Bashforth–Moulton schemes in time [30,31], quasi-spectral in space and fixed-time fourth-order Runge–Kutta scheme in time [27–29], finite elements and finite differences [7,10,19], Padé approximants [23,33], modified equations [35], particle schemes based on the dispersive-velocity method [6], Hermite wavelet methods [22], cell-average based neural network methods [5], and even WENO finite volume methods [2]. In the majority of these numerical methods the addition of artificial viscosity is a requirement in order to cope with solutions with multiple compactons and anticompactons; otherwise, instabilities appear which may cause a blow up of the solution. Numerically-induced phenomena are observed in simulations with numerical methods requiring hyperviscosity, including damping, tails, and dissipative plateaus. They can be studied and corrected by means of the method of modified equations, which properly interprets the truncation error terms of the numerical method as a perturbation of the original evolution equation [11,17,35,41]. For equations with solitary waves, these phenomena adiabatically perturb the parameters of these solutions. The corresponding evolution equations for these parameters can be obtained by perturbation methods, extensively reviewed by Kivshar and Malomed [21]; among these methods, the simplest one is the so-called adiabatic perturbation theory, widely used for a large variety of problems [1,3,8,15,16,18,20,24,25,39]. This technique is based on the slow evolution in time of the invariants of the equation under the perturbation. It can describe the damping in amplitude, the change in speed, the formation of tails and plateaus, and other numerically-induced dissipative phenomena. In evolution equations with compactons, the adiabatic invariant theory has been applied to the propagation of one compacton for the $K(p,p)$ equation [12,36] and the $|K|(p,p)$ equation [14].

In this paper, a numerical implementation of the adiabatic perturbation theory is introduced and applied to solutions with multiple compactons for the $|K|(p,p)$ equation. In Section 2 the compacton solution and the invariants of the $|K|(p,p)$ equation are presented. The adiabatic perturbation theory is applied to this equation in Section 3. The numerical method for the simulations of the $|K|(p,p)$ equation and the numerical implementation of the adiabatic perturbation technique are described in Section 4. Our main results are presented in Section 5, for one compacton in Section 5.1, for compacton trains in Section 5.3, for compacton–compacton chase collisions in Section 5.4, and for compacton–anticompacton chase collisions in Section 5.5. Finally, in Section 6, our main conclusions and future lines of research are presented.

2. Absolute $|K|(p,p)$ equation

Let us consider the absolute Rosenau–Hyman $|K|(p,p)$ equation [13,14], given by

$$u_t - c_0\,u_x + (|u|^{p-1}\,u)_x + (|u|^{p-1}\,u)_{xxx} = 0, \tag{2}$$

where $p > 1$ and c_0 is a constant speed in order to stop one compacton in a moving frame of reference with periodic boundary conditions. The compacton solution of this equation is given by

$$u_c(\xi) = \begin{cases} \operatorname{sign}(c)\left(\frac{2|c|\,p}{p+1}\,\cos^2\left(\frac{p-1}{2\,p}\,\xi\right)\right)^{1/(p-1)}, & |\xi| \le \frac{p\,\pi}{p-1}, \\ 0, & \text{otherwise.} \end{cases} \tag{3}$$

where c is the speed, that determines its maximum amplitude, and $\xi = x - (|c| - c_0)\,t - \xi_0$, with ξ_0 the initial position; note that all the compactons have a fixed width $w_p = 2\,\pi\,p/(p-1)$. Eq. (3) is a compacton for $c > 0$ and an anticompacton for $c < 0$, although both propagates with speed $|c|$; hence, the head-on collisions between compactons and anticompactons observed in the $K(p,p)$ equation for integer even p are not possible in the $|K|(p,p)$ equation, that only allows chase collisions. Eq. (3) is a classical solution of Eq. (2) when $1 < p < 3$, otherwise it is a weak solution, since for $p \ge 3$ the third-order derivative of $|u_c|^{p-1}\,u_c$ is discontinuous at the compacton edges. It should be emphasized that the compacton $u_c(\xi)$ has $\lceil (3-p)/(p-1) \rceil$ continuous derivatives for $p > 1$; hence, it has no continuous derivatives for $p \ge 3$, and only one continuous derivative for $2 \le p < 3$.

The $|K|(p,p)$ equation has four local invariants [14] given by

$$I_1 = \int u\,dx, \qquad I_2 = \int \frac{|u|^{p+1}}{p+1}\,dx, \qquad I_3 = \int \cos(x)\,u\,dx, \qquad I_4 = \int \sin(x)\,u\,dx, \tag{4}$$

and one non-local invariant written as

$$I_{nl} = \int u\,(1 + D_x^2)^{-1}\,u\,dx = \int u\,w\,dx, \qquad w_{xx} + w = u, \tag{5}$$

where $D_x u = u_x$, and

$$w = \sin(x) \int_{-\infty}^{x} \cos(y)\, u(y)\, dy - \cos(x) \int_{-\infty}^{x} \sin(y)\, u(y)\, dy.$$

The invariants I_1, I_{nl}, and I_2 can be interpreted as a generalized mass, a generalized momentum (since its origin is invariance under space translation), and a generalized energy (since its origin is invariance under time translation), respectively [43].

3. Adiabatic perturbation theory

An adiabatic perturbation theory can be applied to study the effect of the hyperviscosity parameter on the numerical propagation of a compacton (or an anticompacton). The $|K|(p,p)$ equation with hyperviscosity, written as

$$u_t - c_0\, u_x + (|u|^{p-1}\, u)_x + (|u|^{p-1}\, u)_{xxx} + \varepsilon\, u_{xxxx} = 0, \tag{6}$$

conserves the first invariant I_1, but slowly changes all the rest of invariants. The evolution equation for the adiabatic change of the second invariant I_2, referred to as $I_{2\varepsilon}(t)$, can be obtained by integration of Eq. (6) after multiplication by $|u|^{p-1}\, u$, resulting in

$$\frac{d\, I_{2\varepsilon}(t)}{dt} \equiv \frac{d}{dt} \int \frac{|u|^{p+1}}{p+1}\, dx = -\varepsilon \int |u|^{p-1}\, u\, u_{xxxx}\, dx, \tag{7}$$

where the following equations have been used:

$$|u|_t = \frac{u}{|u|}\, u_t, \qquad \frac{d}{dt}|u|^{p+1} = (p+1)\, |u|^p\, \frac{u}{|u|}\, u_t,$$

$$-c_0 \int |u|^{p-1}\, u\, u_x\, dx = -\frac{c_0}{p+1} \int (|u|^{p+1})_x\, dx = 0,$$

$$\int |u|^{p-1}\, u\, (|u|^{p-1}\, u)_x\, dx = \frac{1}{2} \int (|u|^{2\,p})_x\, dx = 0,$$

and

$$\int |u|^{p-1}\, u\, (|u|^{p-1}\, u)_{xxx}\, dx = \frac{1}{2} \int \left(\left((|u|^{p-1}\, u)_x \right)^2 \right)_x\, dx = 0.$$

Eq. (7) can be exactly solved for the propagation of one compacton (3). The initial position ξ_0 of the compacton remains constant, but its speed c slowly varies in time, $c(\tau)$, with $\tau = \varepsilon\, t$. The evolution equation for $c(\tau)$ can be obtained by introducing Eq. (3) into Eq. (7), and integrating the support of the compacton, resulting in

$$\frac{d}{d\tau} \int_{-\tilde{\xi}}^{\tilde{\xi}} |u_c|^{p+1}\, d\xi = -(p+1) \int_{-\tilde{\xi}}^{\tilde{\xi}} |u_c|^{p-1}\, u_c\, u_{c,\xi\xi\xi\xi\xi}\, d\xi. \tag{8}$$

with $\tilde{\xi} = p\,\pi/(p-1)$. By straightforward integration, Eq. (8) yields

$$\frac{d}{d\tau} c(\tau) = -\frac{(p-1)^3\, (p^2 - 3\,p - 1)}{(p-5)\, p^3\, (p+3)}\, c(\tau), \tag{9}$$

which is applicable for $1 < p < 5$, since the right-hand side of this equation becomes infinite for $p = 5$. The solution of Eq. (9) is

$$c(\tau) = \exp\left(-\frac{(p-1)^3\, ((p-3)\, p - 1)}{(p-5)\, p^3\, (p+3)}\, \tau \right) c(0). \tag{10}$$

The corresponding change in the second invariant is

$$I_{2\varepsilon}(t) \equiv I_2(\tau) = I_2(0)\, c(\tau)^{(p+1)/(p-1)}. \tag{11}$$

Table 1 shows the expression for the speed $c(\tau)$ of one compacton and its second invariant $I_2(\tau)$ for the $|K|(p,p)$ equation with $p = 1.5, 2, \ldots, 5$. Both $c(\tau)$ and $I_2(\tau)$ monotonically decrease for $p < (3 + \sqrt{13})/2 \approx 3.303$, but monotonically grow otherwise.

In general, the solution $I_{2\varepsilon}(t)$ of Eq. (7) for an arbitrary solution $u(x,t)$ of the $|K|(p,p)$ equation will not be monotonic. Such a result is expected for compacton–compacton and compacton-anticompacton chase collisions. The soliton resolution conjecture applied to the $|K|(p,p)$ equation suggest that its general solution will decompose into a series of compactons and anticompactons over a radiation background. Hence, for the evaluation of the right-hand side of Eq. (7), it should be taking into account that the compacton solution of the $|K|(p,p)$ equation satisfies that $u_c(x,\cdot) \in \mathrm{C}^4$ for $1 < p < 3/2$, $u_c \in \mathrm{C}^3$ for $p < 5/3$, $u_c \in \mathrm{C}^2$ for $p < 2$, $u_c \in \mathrm{C}^1$ for $p < 3$, and $u_c \in \mathrm{C}^0$ for $p \geq 3$; furthermore, $|u_c|^{p-1}\, u_c \in \mathrm{C}^3$ for $p < 3$. Hence, the fourth-order derivative u_{xxxx} in Eq. (7) requires

Table 1
The compacton speed $c(\tau)$ and the second invariant $I_2(\tau)$ for the $|K|(p,p)$ equation with $p = 1.5, 2, \ldots, 4.5$, obtained by evaluation of from Eqs. (10) and (11), respectively.

p	$c(\tau)$	$I_2(\tau)$
1.5	$\exp(-13\,\tau/1701)\,c(0)$	$\exp(-65\,\tau/1701)\,I_2(0)$
2	$\exp(-\tau/40)\,c(0)$	$\exp(-3\,\tau/40)\,I_2(0)$
2.5	$\exp(-243\,\tau/6875)\,c(0)$	$\exp(-567\,\tau/6875)\,I_2(0)$
3	$\exp(-2\,\tau/81)\,c(0)$	$\exp(-4\,\tau/81)\,I_2(0)$
3.5	$\exp(125\,\tau/4459)\,c(0)$	$\exp(225\,\tau/4459)\,I_2(0)$
4	$\exp(81\,\tau/448)\,c(0)$	$\exp(135\,\tau/448)\,I_2(0)$
4.5	$\exp(7889\,\tau/10935)\,c(0)$	$\exp(12397\,\tau/10935)\,I_2(0)$

that $p < 3/2$. In order to avoid such a limitation, it can be taken advantage of the fact that, by application of the integration by parts, for a regular enough solution, the following expressions are analytically equivalent

$$\int |u|^{p-1}\,u\,u_{xxxx}\,dx = -\int (|u|^{p-1}\,u)_x\,u_{xxx}\,dx = \int (|u|^{p-1}\,u)_{xx}\,u_{xx}\,dx = -\int (|u|^{p-1}\,u)_{xxx}\,u_x\,dx = \int (|u|^{p-1}\,u)_{xxxx}\,u\,dx. \tag{12}$$

Therefore, it is recommended that Eq. (7) will be written as

$$\frac{dI_{2\varepsilon}}{dt} = \varepsilon \int (|u|^{p-1}\,u)_{xxx}\,u_x\,dx. \tag{13}$$

The right-hand side of this equation is finite for classical solutions of the $|K|(p,p)$ equation, i.e., for $p < 3$; in this paper, it will be also used for $p > 3$.

4. Numerical methods

The simulations of the solutions of the $|K|(p,p)$ equation in this paper have been obtained by means of a finite element method based on a Petrov–Galerkin formulation. We use piecewise linear test functions, cubic B-splines as trial functions, the product approximation for the nonlinear terms, and periodic boundary conditions [4,7,33]. This method results in the system ordinary differential equations given by

$$\mathcal{A}(\mathrm{E})\,\frac{dU_j}{dt} - c_0\,\mathcal{B}(\mathrm{E})\,U_j + \big(\mathcal{B}(\mathrm{E}) + \mathcal{C}(\mathrm{E})\big)\,(|U_j|^{p-1}\,U_j) + \varepsilon\,\mathcal{D}(\mathrm{E})\,U_j = 0, \tag{14}$$

where $U_j(t) = U(x_j,t) \approx u(x_j,t)$, a uniform mesh is used in space $x_j = x_0 + j\,\Delta x$, with $j = 0, 1, \ldots, N$, and the matrices can been written in a compact format by using difference operators given by

$$\mathcal{A}(\mathrm{E}) = \frac{\mathrm{E}^{-2} + 26\,\mathrm{E}^{-1} + 66 + 26\,\mathrm{E}^{1} + \mathrm{E}^{2}}{120}, \qquad \mathcal{B}(\mathrm{E}) = \frac{-\mathrm{E}^{-2} - 10\,\mathrm{E}^{-1} + 10\,\mathrm{E}^{1} + \mathrm{E}^{2}}{24\,\Delta x},$$

$$\mathcal{C}(\mathrm{E}) = \frac{-\mathrm{E}^{-2} + 2\,\mathrm{E}^{-1} - 2\,\mathrm{E}^{1} + \mathrm{E}^{2}}{2\,\Delta x^3}, \qquad \mathcal{D}(\mathrm{E}) = \frac{\mathrm{E}^{-2} - 4\,\mathrm{E}^{-1} + 6 - 4\,\mathrm{E}^{1} + \mathrm{E}^{2}}{\Delta x^4},$$

with the shift operator E defined such that $\mathrm{E}\,U_j = U_{j+1}$, and $\mathrm{E}^{-1}\,U_j = U_{j-1}$.

For the integration in time of Eq. (14), the implicit midpoint rule is used, resulting in

$$\mathcal{A}(\mathrm{E})\,\frac{U_{j,m+1} - U_{j,m}}{\Delta t} - (c_0\,\mathcal{B}(\mathrm{E}) - \varepsilon\,\mathcal{D}(\mathrm{E}))\left(\frac{U_{j,m+1} + U_{j,m}}{2}\right) + (\mathcal{B}(\mathrm{E}) + \mathcal{C}(\mathrm{E}))\left(\left|\frac{U_{j,m+1} + U_{j,m}}{2}\right|^{p-1}\left(\frac{U_{j,m+1} + U_{j,m}}{2}\right)\right) = 0. \tag{15}$$

where $U_{j,m} = U_j(t_m) \approx u(x_j,t_m)$, with $t_m = m\,\Delta t$, $m = 0, 1, \ldots, M$, for a fixed timestep numerical integration. The nonlinear equation (15) is solved by means of Newton's iterative method with an absolute tolerance error of $\mathrm{TOL} = 10^{-10}$ as stopping criterion. Method (15) is second-order accurate in space for $\varepsilon > 0$, although it is fourth-order accurate for $\varepsilon = 0$, and second-order accurate in time, being (linearly) unconditionally stable [19,33]. The computational complexity of this numerical algorithm is linear in both the number of grid nodes and the number of timesteps, $O(N\,M)$; in fact, the Newton's method used in each time step converges in less than five iterations. The algorithm has been implemented in Matlab and executed on multiple laptop and desktop computers; the most powerful one is an Intel Core i5-13500 processor with a base clock speed of 2.5 GHz, a turbo boost up to 4.8 GHz, and 32 GB of high-speed DDR5 RAM. We execute an instance of the code in every core of the machine, resulting in a typical time for simulation of several hours, depending on the grid size and the timestep.

The invariants of the $|K|(p,p)$ equation will be numerically evaluated by means of the trapezoidal rule (recommended for periodic functions in Ref. [40]),

$$I_{1,m} = \Delta x \sum_{j=0}^{N} U_{j,m}, \qquad I_{2,m} = \Delta x \sum_{j=0}^{N} \frac{|U_{j,m}|^{p+1}}{p+1}, \quad m = 0, 1, \ldots, M.$$

By using these expressions, the numerical method (15) without hyperviscosity ($\varepsilon = 0$) conserves the first invariant by construction; however, the second invariant is not conserved.

Table 2
The variation in the first and second invariants of a $|K|(2,2)$ equation for the propagation of one compacton with speed c as a function of c_0 and ε by using $\Delta x = 0.01$, $\Delta t = 0.002$, $x \in [0, 250]$, and $t \in [0, 200]$, and TOL $= 10^{-10}$. The $^{(*)}$ indicates that the value corresponds to $|I_i(0) - I_i(79)|$, $i = 1, 2$.

c_0	$\lvert I_1(0) - I_1(200)\rvert$	$\lvert I_2(0) - I_2(200)\rvert$	$\lvert I_1(0) - I_1(200)\rvert$	$\lvert I_2(0) - I_2(200)\rvert$
	$\varepsilon = 0$		$\varepsilon = 10^{-5}$	
0	$4.7 \cdot 10^{-12\ (*)}$	$2.1 \cdot 10^{-11\ (*)}$	$2.4 \cdot 10^{-10}$	$4.7 \cdot 10^{-4}$
0.1	$1.2 \cdot 10^{-11}$	$5.5 \cdot 10^{-11}$	$3.7 \cdot 10^{-12}$	$4.7 \cdot 10^{-4}$
0.5	$2.7 \cdot 10^{-12}$	$2.8 \cdot 10^{-12}$	$1.4 \cdot 10^{-10}$	$4.7 \cdot 10^{-4}$
1	$3.7 \cdot 10^{-12}$	$1.1 \cdot 10^{-11}$	$2.2 \cdot 10^{-10}$	$4.7 \cdot 10^{-4}$

A numerical implementation of the adiabatic perturbation theory allows the comparison between the numerical evolution of the second invariant and its adiabatic prediction in solutions with multiple compactons. Eq. (13) will be numerically solved by the second-order trapezoidal method (equivalent to a quadrature with the trapezoidal rule),

$$I_{2\varepsilon,m+1} = I_{2\varepsilon,m} + \Delta t\,(i_{\varepsilon,m+1} + i_{\varepsilon,m})/2, \qquad I_{2\varepsilon,0} = I_{2,0}, \tag{16}$$

with

$$i_{\varepsilon,m} = \varepsilon\,\Delta x \sum_{j=0}^{N} V_{xxx,j,m}\,U_{x,j,m},$$

where the third- and first-order spatial derivatives has been approximated by

$$\mathcal{A}(\mathrm{E})\,V_{xxx,j,m} = C(\mathrm{E})\,(|U_{j,m}|^{p-1}\,U_{j,m}), \qquad \mathcal{A}(\mathrm{E})\,U_{x,j,m} = \mathcal{B}(\mathrm{E})\,U_{j,m}.$$

Note that, for classical solutions, i.e., $1 < p < 3$, these approximations are fourth-order accurate.

5. Presentation of results

The main goal of this paper is the assessment of the numerical implementation of the adiabatic perturbation theory for the study of the evolution of the second invariant in solutions with multiple compactons for the $|K|(p,p)$ equation. In Section 5.1 its evolution during the numerical propagation of one compacton of the $|K|(2,2)$ equation is studied as a function of c_0, ε, and $\Delta x/\Delta t$. In Section 5.2 the adiabatic perturbation theory is applied to the one-compacton solution of the $|K|(p,p)$ equation. Its evolution for initial conditions that generate multiple compactons for the $|K|(2,2)$ equation is analyzed in Section 5.3. Compacton–compacton chase collisions and compacton–anticompacton chase collisions for the $|K|(p,p)$ equation are considered in Sections 5.4 and 5.5, respectively.

5.1. One compacton of the $|K|(2,2)$ equation

Let us begin illustrating the general features observed in the propagation of one compacton solutions with and without hyperviscosity. Table 2 shows the variation of the first and second invariants in the propagation of one compacton with $c = 1$, for $c_0 = 0$, 0.1, 0.5, and 1, without hyperviscosity ($\varepsilon = 0$) and with small hyperviscosity (10^{-5}), both with $\Delta x/\Delta t = 5$. Without hyperviscosity ($\varepsilon = 0$), the second invariant for $c_0 > 0$ is well conserved, with variations in its value of the same order in magnitude to those observed for the first invariant. However, for $c_0 = 0$ an instability appears; until $t = 79$ the second invariant is well conserved, as indicated by the values marked with $^{(*)}$ in the table, but then it starts to grow until it blows up. The table also illustrates that for a typical value of the hyperviscosity in the study of compacton-anticompacton chase collisions, $\varepsilon = 10^{-5}$, the second invariant evolves following the analytical adiabatic perturbation theory presented in Section 3. Specifically, $I_{2\varepsilon}(t) - I_2(0) = (\exp(-3\,\varepsilon\,t/40) - 1)\,I_2(0)$ as shown in Table 1; hence, the value in the last column of Table 2 can be predicted by the approximation $|I_2(200) - I_2(0)| \approx 15\,\varepsilon\,I_2(0) = 4.7 \cdot 10^{-4}$, being independent of c_0.

An instability like the one observed in Table 2 for $c_0 = 0$ and $\varepsilon = 0$ is usually associated to the violation of the Courant–Friedrichs–Lewy (CFL) condition. It states that, for the stability and convergence of a numerical method, it is necessary that the numerical speed $\Delta x/\Delta t$ be larger than the propagation speed of the solution. For one compacton with speed $c > 0$ in a moving frame with c_0, this condition requires that the numerical speed $\Delta x/\Delta t \geq |c - c_0|$. Let us recall that the numerical simulations of one compacton of the $K(2,2)$ equation are accompanied by numerically-induced radiation [14,33,34]; precisely, forward and backward wavepackets of radiation propagating with group velocities $6\,c_0$ and 0, respectively, have been reported (note that these group velocities are $5\,c_0$ and $-c_0$ in the reference frame moving at c_0). Similar phenomena are expected for the $|K|(2,2)$ equation; hence, the CFL condition should be $\Delta x/\Delta t \geq \max\{|c - c_0|, 5\,|c_0|\}$. However, in Ref. [34], it was shown that the origin of the self-similar radiations for the $K(2,2)$ equation is the numerical approximation to the linear c_0 term; thus, these radiations should be absent for $c_0 = 0$.

Further exploration of the potential role of the CFL condition in the instability of the one compacton solution observed in Table 2 for $c_0 = 0$ and $\varepsilon = 0$ is required. Fig. 1 shows the evolution in time of $|I_2(t) - I_2(0)|$ the for such a solution with $\Delta x/\Delta t = 5$ (blue line marked with squares), 5.1 (yellow line with stars), 5.2 (green line with circles), and 20 (red line with triangles), the first three ones

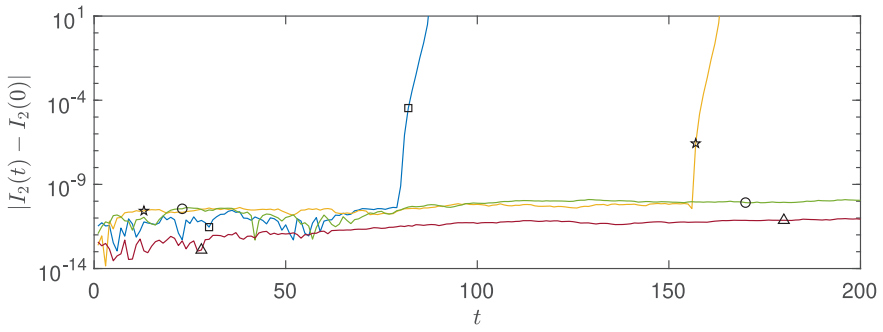

Fig. 1. The variation of the second invariant $|I_2(t) - I_2(0)|$ for the propagation of one compacton of the $|K|(2,2)$ equation with $c = 1$ and $c_0 = 0$, for $\Delta x = 0.01$, with $\Delta t = \Delta x/5$ (blue line), $\Delta x/5.1$ (yellow line), and $\Delta x/5.2$ (green line), and for $\Delta x = 0.02$, with $\Delta t = \Delta x/20$ (red line), all with $\epsilon = 0$, $x \in [0, 250]$, and TOL $= 10^{-10}$. (For easy interpretation of the references to color in this figure, the blue line is marked with two squares, the yellow one with stars, the green one with circles, and the red one with triangles). (For interpretation of the references to color in this figure legend, the reader is referred to the web version of this article.)

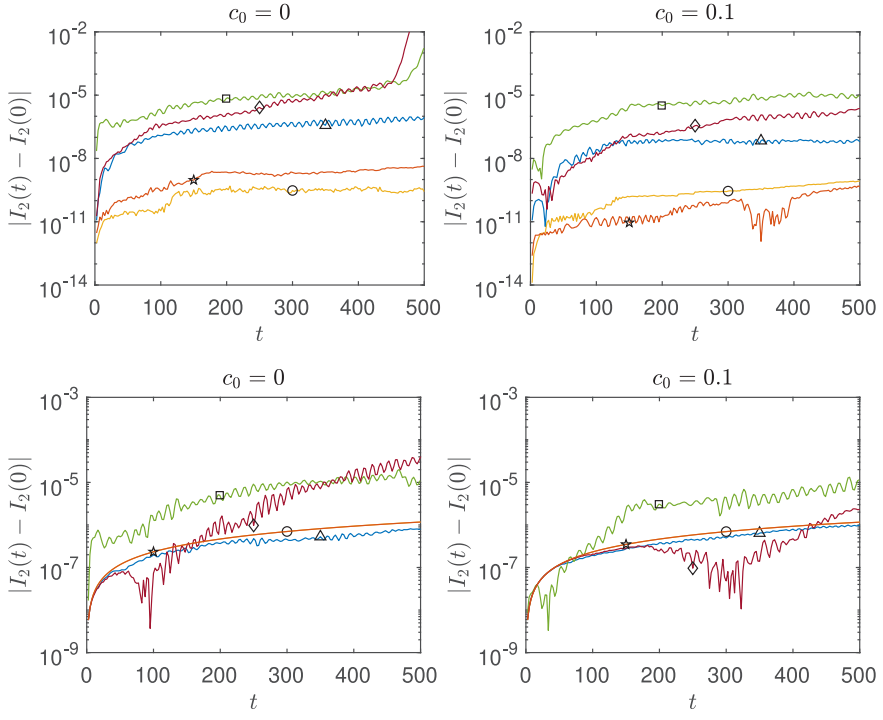

Fig. 2. The variation of the second invariant $|I_2(t) - I_2(0)|$ for the propagation of one compacton of the $|K|(2,2)$ equation with $c = 1$, $c_0 = 0$ (left panels) and $c_0 = 0.1$ (right panels), $\epsilon = 0$ (top panels) and $\epsilon = 10^{-8}$ (bottom panels), for $\Delta x/\Delta t = 10$ (yellow line), 5 (orange line), 2 (blue line), 1 (red line), and 0.5 (green line), with $\epsilon = 0$, $t \in [0, 500]$, $\Delta x = 0.1$, and $\Delta t = 0.01$, 0.02, 0.05, 0.1, and 0.2. (For easy interpretation of the references to color in this figure, the yellow line is marked with a circle, the orange one with a star, the blue one with a triangle, the red one with a diamond, and the green one with a square.). (For interpretation of the references to color in this figure legend, the reader is referred to the web version of this article.)

with $\Delta x = 0.01$, but the last one with $\Delta x = 0.02$. The blow-up instability is observed in the panels for $\Delta x/\Delta t = 5$ (starting at $t = 79$) and 5.1 (at $t = 156$). However, for $\Delta x/\Delta t = 5.2$ and 20 the second invariant is well conserved, with no instability. Apparently, the CFL condition is $\Delta x/\Delta t > 5.1$ for $c_0 = 0$ in this simulations.

Fig. 2 shows the variation of the second invariant for one compacton with $c = 1$, with $c_0 = 0$ (left panels) and $c_0 = 0.1$ (right panels), $\epsilon = 0$ (top panels), and $\epsilon = 10^{-8}$ (bottom panels), with $\Delta x/\Delta t = 10$ (yellow line marked with a circle), 5 (orange line with a star), 2 (blue line with a triangle), 1 (red line with a diamond), and 0.5 (green line with a square), with $\Delta x = 0.1$. In the top left panel, for $c_0 = 0$ and $\epsilon = 0$, the second invariant is well-conserved for $\Delta x/\Delta t = 10$ (yellow line) and 5 (orange line), although it grows two orders of magnitude in the timespan. In the cases $\Delta x/\Delta t = 1$ (red line) and 0.5 (green line) the solution becomes unstable before $t = 500$. However, for $\Delta x/\Delta t = 2$ (blue line) the result is not conclusive, but apparently a behavior similar to that of 0.5 is expected for times larger than the timespan in the plot.

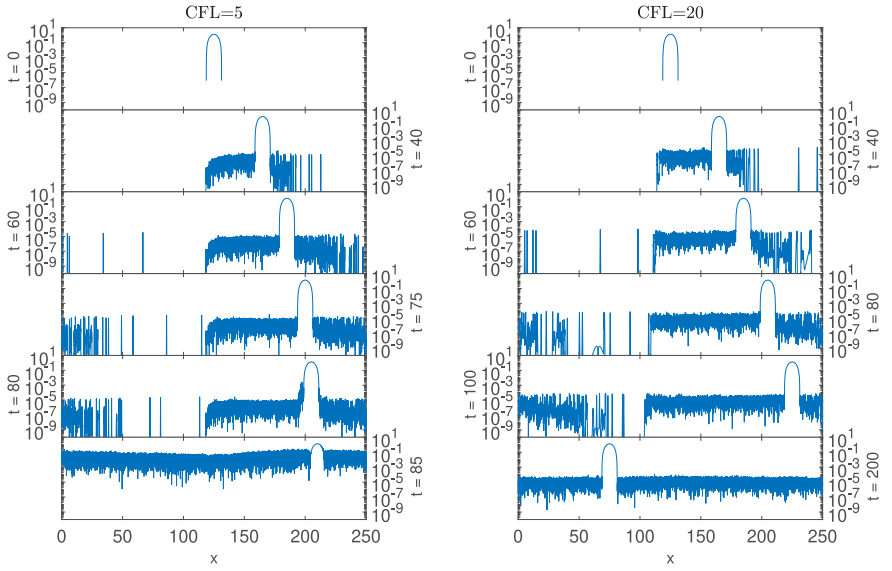

Fig. 3. The propagation of a numerical compacton with $c = 1$ and $c_0 = 0$ for the $|K|(2,2)$ equation with either $\Delta x = 0.01$ and $\Delta t = 0.002$ (left column, entitled CFL = 5), or $\Delta x = 0.02$ and $\Delta t = 0.001$ (right column, entitled CFL=20), both with $\varepsilon = 0$, $x \in [0, 250]$, and TOL $= 10^{-10}$.

In the top right panel of Fig. 2, for $c_0 = 0.1$ and $\varepsilon = 0$, the second invariant is also well-conserved for $\Delta x/\Delta t = 10$ (yellow line) and 5 (orange line), but reaches very large values for 2 (blue line), 1 (red line), and 0.5 (green line), although without the instability inside the timespan observed for $c_0 = 0$.

In the bottom left panel of Fig. 2, for $c_0 = 0$ and $\varepsilon = 10^{-8}$, the most noticeable feature is that the results for $\Delta x/\Delta t = 10$ (yellow line) and 5 (orange line) overlap up to the plot resolution and follow the prediction of the adiabatic perturbation theory for the evolution of the second invariant. The result for $\Delta x/\Delta t = 2$ (blue line) also follows it, but with some oscillations. The second invariant for $\Delta x/\Delta t = 1$ (red line) initially follows the adiabatic perturbation until $t = 20$, but at $t = 100$ begins to grow about three orders of magnitude. In the last case for $\Delta x/\Delta t = 0.5$ (green line) the disagreement with the perturbative prediction already starts at the first timesteps.

Finally, in the bottom right panel of Fig. 2, for $c_0 = 0.1$ and $\varepsilon = 10^{-8}$ with $\Delta x/\Delta t = 10$ (yellow line), 5 (orange line), and 2 (blue line) the second invariant follows the dynamics predicted by adiabatic perturbations based on the hyperviscosity. However, for $\Delta x/\Delta t = 1$ (red line) and 0.5 (green line) there are deviations starting at $t = 80$ and at the first timesteps, respectively.

The results in Fig. 2 suggest that there are numerically-induced phenomena in the simulations of the $|K|(2,2)$ equation for $c_0 = 0$ beyond the forward and backward self-similar radiations observed for the $K(2,2)$ equation with $c_0 > 0$ in Ref. [34]. In order to clarify such phenomena, Fig. 3 shows the propagation of a compacton with speed $c = 1$ in a rest frame $c_0 = 0$ for $\Delta x/\Delta t = 5$ (left panel) and 20 (right panel), corresponding to the invariants plotted with blue and red lines, resp., in Fig. 1. In both cases forward and backward radiations are emitted by the compacton; however, they are not self-similar. It should be remarked that simulations with $c_0 = 0$ for the $K(2,2)$ equation blow up in the first few timesteps. The robustness of the $|K|(2,2)$ equation allows stable simulations for $c_0 = 0$, but losing the self-similarity of the radiations.

Fig. 3 left panel, for $\Delta x/\Delta t = 5$, shows that the backward radiation remains nearly at rest, with a very slow speed of -0.0042. But the forward radiation emits thin wavepackets with the maximum wavenumber ($k = \pi/\Delta x$), as shown in the left panel at $t = 40$. A careful follow up of these wavepackets show that their group velocity is between 2 and 7, linearly depending on the amplitude of their envelope. Hence, the CFL condition do not holds for these thin wavepackets. Moreover, they reenter the domain and reach the position of the left front of the backward radiation at $t \approx 67.5$ (not illustrated in the panels). In the left panel at $t = 75$, it can be observed that the thin wavepackets have a larger amplitude than the backward radiation. The instability associated to the CFL condition starts at $t = 79$, cf. Table 2, when the leading thin wavepacket reaches the left side of the compacton (illustrated in the left panel with $t = 80$ as a sharp front over the backward radiation at $x \approx 195$). Subsequently, the amplitude of both radiations start to grow until the solution blows up (in the figure this behavior is illustrated with the panel at $t = 120$ where the radiation nearly reaches the amplitude of the compacton). This instability is the one observed in Fig. 1 (blue curve marked with squares) for the second invariant.

Fig. 3 right panel, for $\Delta x/\Delta t = 20$, shows that the backward radiation moves with a slow speed of -0.14 and the forward radiation emits thin wavepackets with a group velocity between 3 and 5, also linearly depending on their amplitude (see right panels at $t = 40$, 60, and 80). The first wavepacket (peak in the figure) moves with a group velocity of 4.1 at $t = 40$, accelerating up to 5.1, a speed that remains constant at $t = 60$ and 80 (in the panel at $t = 100$ this peak is over the backward radiation, being difficult to see). This wavepacket reenter the domain and reach the position of the left front of the backward radiation at $t \approx 62.5$, reaching the left side

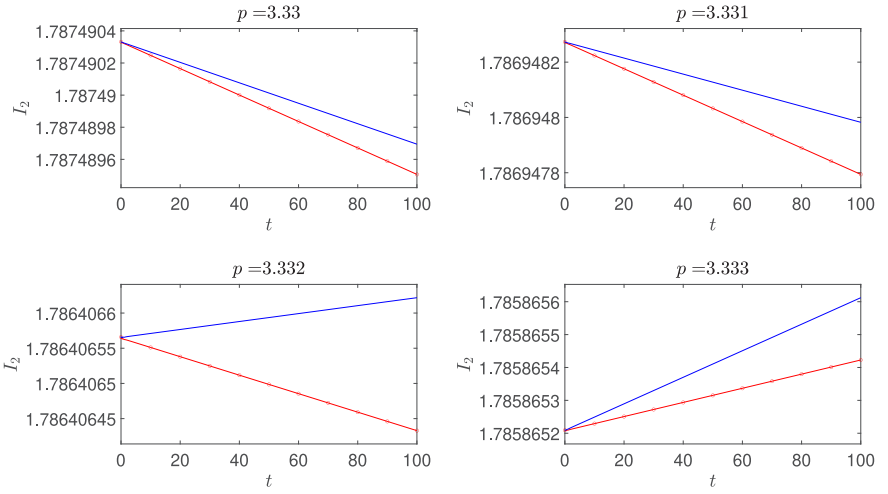

Fig. 4. Evolution of the second invariant $I_2(t)$ (blue curve) and the prediction of the numerical adiabatic perturbation theory for $I_{2\varepsilon}(t)$ (red curve with circles) in the propagation of one compacton for the $|K|(p,p)$ equation with $p = 3.33$ (top left panel), 3.331 (top right), 3.332 (bottom left), and 3.333 (bottom right), for $c = 1 = c_0$ with $\varepsilon = 10^{-5}$, $\Delta x/\Delta t = 5$, $\Delta x = 0.01$, and $\Delta t = 0.002$. (For interpretation of the references to color in this figure legend, the reader is referred to the web version of this article.)

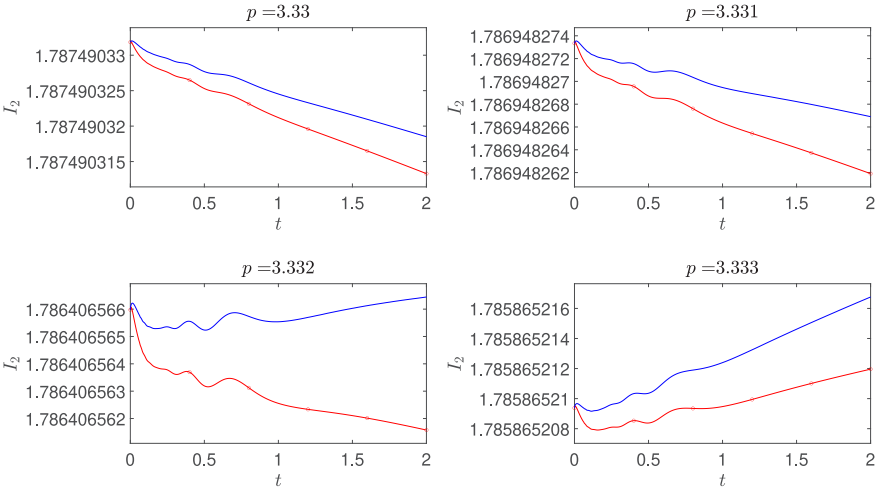

Fig. 5. Zoom in $t \in [0,2]$ of the plots on the evolution of the second invariant in Fig. 4.

of the compacton at $t \approx 79.5$ without any noticeable feature (see the panel at $t = 80$). No instability is produced, as observed in the panels at $t = 100$ and 200, and in the second invariant plotted in Fig. 1 (red curve marked with triangles).

The results shown in Fig. 3 suggests that the maximum speed of the thin wavepackets emitted by the forward radiation have a speed of 5.14, hence for a stable simulation the CFL condition should be $\Delta x/\Delta t > 5.14$. This analysis explains the results plotted in Fig. 1, where $\Delta x/\Delta t = 5.2$ yields a stable simulation, but $\Delta x/\Delta t = 5.1$ results in the blow up of the solution. Currently, we have no explanation to the appearance of the thin wavepackets from the forward radiation, and to the lack of self-similarity of the forward and backward radiations for $c_0 = 0$. Future research is required to explain the origin of these numerically-induced phenomena.

5.2. One compacton of the $|K|(p,p)$ equation

The numerical simulations of the propagation of one compacton for the $|K|(p,p)$ equation with $p = 1.5$, 2.5, 3.5, and 4.5 show an excellent agreement between the evolution of the second invariant and the analytical prediction of the adiabatic perturbation theory. However, there is a disagreement for p around the critical value $p_{cr} = (3 + \sqrt{13})/2 \approx 3.303$ that separates the region in which the analytical adiabatic perturbation theory predicts that the second invariant decreases in time, $p < p_{cr}$, or increases in time, otherwise.

Fig. 4 shows the second invariant $I_2(t)$ (blue curve) and its numerical adiabatic prediction $I_{2\varepsilon}(t)$ (red curve marked with circles) for the propagation of one compacton of the $|K|(p,p)$ equation with $p = 3.33$ (top left panel), 3.331 (top right), 3.332 (bottom left),

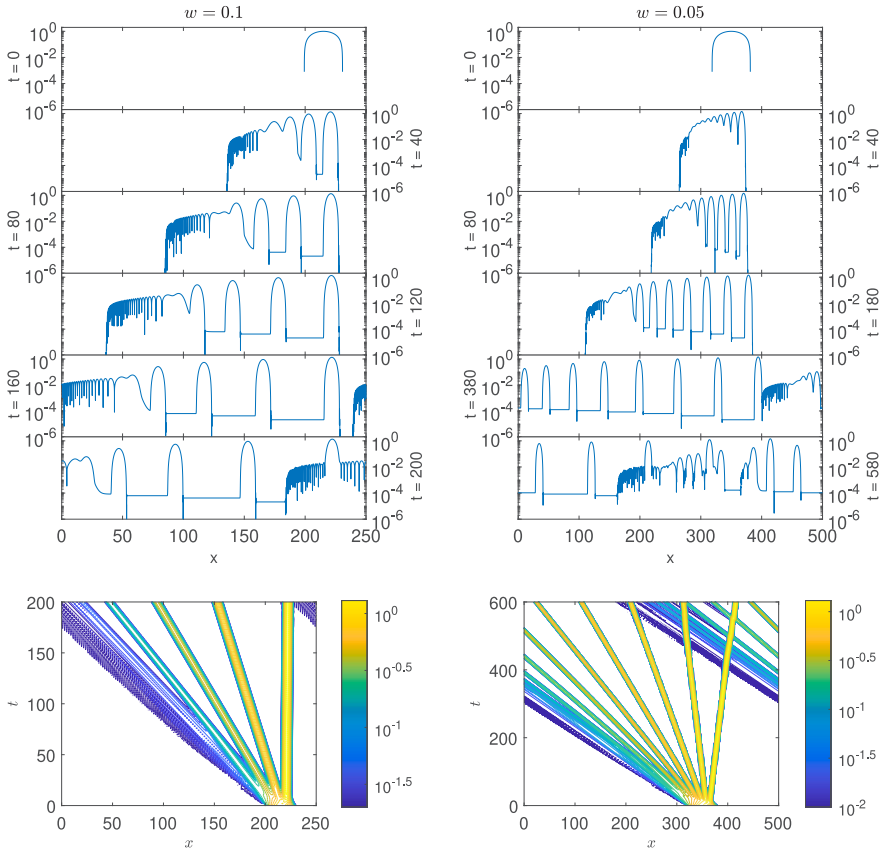

Fig. 6. The generation of a compacton train from a truncated cosine as an initial condition for the $|K|(2,2)$ equation with a frequency of $\tilde{\omega} = 0.1$ (left panels) and 0.05 (right panels), with the corresponding contour plots (bottom panels). In the left panels, the simulations use $x_0 = 215$, $c_0 = 1$, $\Delta x = 0.02$, $\Delta t = 0.001$, $\epsilon = 1 \cdot 10^{-4}$, and $x \in [0, 250]$; and in the right panels, they use $x_0 = 380$, $c_0 = 1$, $\Delta x = 0.1$, $\Delta t = 0.01$, $\epsilon = 1 \cdot 10^{-4}$, and $x \in [0, 600]$.

and 3.333 (bottom right), for $c = 1 = c_0$ with $\epsilon = 10^{-5}$. The evolution of $I_2(t)$ in all the panels is approximately linear in time, although the analytical prediction is an exponential behavior in time, due to the tiny exponent. The top panels show that the slope of $I_2(t)$ (blue curves) is $-6.37 \cdot 10^{-9}$ for $p = 3.330$, and $-2.91 \cdot 10^{-9}$ for $p = 3.331$. It should be noticed that the slopes for these values of $p > p_{cr}$ are negative, against the prediction of the analytical adiabatic perturbation theory; moreover, the numerical adiabatic perturbation theory also predicts a negative slope (as illustrated in the top right panel).

The bottom panels in Fig. 4 show that the slope of $I_2(t)$ is positive for $p = 3.332$ and 3.333, specifically, $5.59 \cdot 10^{-10}$ and $4.03 \cdot 10^{-9}$, respectively. However, the numerical adiabatic perturbation theory predicts a negative slope for $p = 3.332$ (bottom left panel) and a positive one for $p = 3.333$ (bottom right panel). By using inverse linear interpolation, we estimate that the change between negative and positive slopes of $I_2(t)$ occurs at $p = 3.3318368 \pm 0.0000008$, but for $I_{2\epsilon}(t)$ occurs at $p = 3.3323790 \pm 0.0000007$, both larger than the analytical prediction p_{cr}. Hence, the adiabatic perturbation theory analytically underpredicts the value of p_{cr}, but numerically overpredicts it; however, in the last case, the estimation has a relative error of only the 0.02%.

We have no rigorous explanation for the mismatch between the adiabatic prediction of the critical value p_{cr} and the numerical results. However, Fig. 5 shows a zoom in the time interval $[0, 2]$ of the plots for $I_2(t)$ (blue curve) and $I_{2\epsilon}(t)$ (red curve with circles) in Fig. 4. It is observed that the numerical invariants oscillate for $t < 1$, with four maxima and three minima, before entering into a monotonic linear evolution. Such transitory oscillations are outside the predictions of the analytical adiabatic perturbation for the evolution of one compacton; we think that they are associated with the emission of the numerically-induced radiation observed in Fig. 3.

5.3. Multiple compactons for the $|K|(2,2)$ equation

The adiabatic perturbation theory can be used to predict the evolution of the second invariant in arbitrary solutions of the $|K|(2,2)$ equation with multiple compactons. In the study of the generation of compacton trains, the most widely used initial condition is a truncated cosine profile, given by

$$u(x,0) = \begin{cases} \cos(\tilde{\omega}(x - x_0)), & \tilde{\omega}|x - x_0| \leq \pi/2, \\ 0, & \text{otherwise.} \end{cases}$$

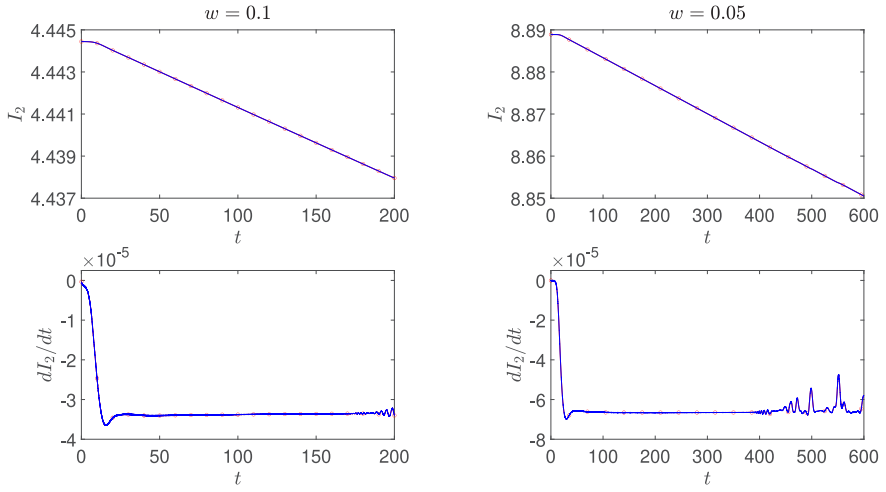

Fig. 7. The evolution of the second invariant (top panels) and its time derivative (bottom panels) for the $|K|(2,2)$ equation (blue line) and the corresponding predictions from adiabatic perturbations (red line with red circles) for the solutions plotted in Fig. 6. (For interpretation of the references to color in this figure legend, the reader is referred to the web version of this article.)

Fig. 6 shows the generation of a compacton train from two truncated cosine initial conditions, one with $\tilde{\omega} = 0.1$ (left panels) and another one with $\tilde{\omega} = 0.05$ (right panels), both with $\epsilon = 1 \cdot 10^{-4}$. For $\tilde{\omega} = 0.1$ (left panels), the initial condition ($t = 0$) generates a train of four compactons in succession, with decreasing amplitudes of 1.35, 0.92, 0.55, and 0.26, values that remain constant from $t = 160$ until $t = 200$, followed by a small zero-mass residual and an oscillatory tail that stretches to the left as time passes. The panel at $t = 0$ shows the initial condition. The first compacton is well-separated from the rest ones at $t = 40$, the second one is in the process of separation, and both are connected by a dissipative plateau. At $t = 80$, $t = 120$, and $t = 160$ the first two, three, and four compactons, respectively, are well-separated from the rest ones, with plateaus of increasing amplitude from the right to the left between them. At $t = 160$, the four compactons are well separated from the residual and its oscillatory tail, that has reentered the domain. Finally, at $t = 200$, the tallest compacton is over the oscillatory tail, without any change on its amplitude. The bottom left panel shows a contour panel with the four compactons in yellow, orange, green–orange, and cyan-white colors, the residual in blue color, and the first part of the oscillatory tail in dark blue (the full oscillatory tail is not represented in this contour panel for clarity).

For $\tilde{\omega} = 0.05$, the right panels in Fig. 6 show that the initial condition (at $t = 0$), which width is exactly the double of that of the one in the right panel, generates a train of eleven compactons of decreasing amplitudes of 1.44, 1.23, 1.01, 0.808, 0.621, 0.453, 0.304, 0.186, 0.104, 0.0858, and 0.0510 (at $t = 580$). At $t = 40$, no compacton is well separated from the rest, with all connected to an emerging oscillatory tail. At $t = 80$ ($t = 180$), the first three (six) compactons are well separated, with plateaus of increasing amplitude from the right to the left, with the fourth (seventh) one in process of separation of the rest ones; simultaneously, the oscillatory tail stretches. At $t = 380$, eight compactons are well separated with plateaus between them and the tallest compacton in contact with the oscillatory tail that has reentered the domain; the remaining smaller compactons are in process of separation near the right boundary of the domain.

Finally, at $t = 580$, in the right panels in Fig. 6, eleven compactons can be observed, with the three smallest one in process of separation; the five smallest compactons (from the eleventh to the seventh) have already collided with the tallest compacton, which is now between the seventh and sixth compactons; the second compacton has collided with the three smallest compactons (from the eleventh to the ninth), being now at the left of the eighth compacton; and the third compacton is over the oscillatory tail, with the residual at the left of the three smallest compactons. The bottom right panel shows a contour panel with the eleven compactons in colors from yellow to blue, and the residual and the first part of the oscillatory tail in dark blue (the whole oscillatory tail is not represented in this contour panel). Let us highlight that, in the contour plot, the slope for the tallest compacton changes in every chase collision with the shortest ones, due to its delay during the interaction (illustrated in the top left part of the bottom right panel).

Fig. 7 illustrates that the prediction of the adiabatic perturbation theory (red curve with circles) for the evolution of the second invariant (blue curve) is in excellent agreement with the numerical results for both the truncated cosine with $\tilde{\omega} = 0.1$ (left panels) and 0.05 (right panels). The second invariant remains nearly constant until $t = 7$ for $\tilde{\omega} = 0.1$ (top left panel) or $t = 17$ for $\tilde{\omega} = 0.05$ (top right panel), where its slope rapidly changes down to $-3.4 \cdot 10^{-5}$ (bottom left panel) or $-6.6 \cdot 10^{-5}$ (bottom right panel). After that large change, the time derivative of the second invariant remains nearly constant until some oscillations appear when the oscillatory tail of the residual touches the leading compacton at $t = 172$ (bottom left panel) or at $t = 380$ (bottom right panel). Even during these oscillations, the prediction of the numerical adiabatic perturbation theory agrees with the numerical results.

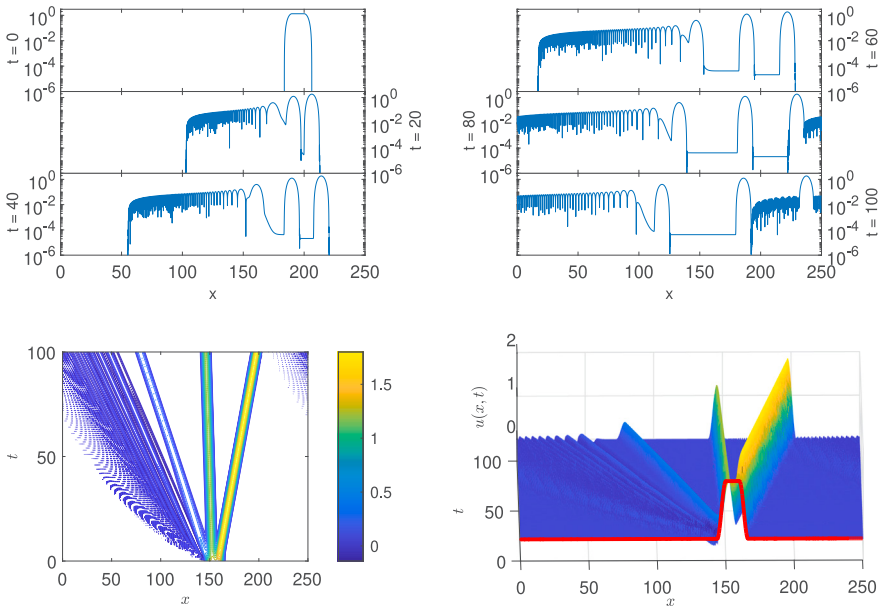

Fig. 8. The generation of a compacton train from a dilated compacton with $c = 1 = c_0$ and $w = 10$ as an initial condition for the $|K|(2,2)$ equation by using $\Delta x = 0.01$, $\Delta t = 0.002$, $\varepsilon = 1 \cdot 10^{-4}$, and $x \in [0, 250]$. The top panels show six time snapshots, and the bottom panels show a contour plot (bottom left panel) and a surface plot with the initial condition in red color (bottom right panel). (For interpretation of the references to color in this figure legend, the reader is referred to the web version of this article.)

Another standard way to study the generation of compacton trains is by using a dilated compacton as an initial condition, given by [14,23,33]

$$u(x,0) = \begin{cases} \frac{4c}{3}\cos^2\left(\frac{x-x_0}{4}\right), & -2\pi \le x - x_0 < 0, \\ \frac{4c}{3}, & 0 \le x - x_0 \le w, \\ \frac{4c}{3}\cos^2\left(\frac{x-x_0-w}{4}\right), & w < x - x_0 \le w + 2\pi, \end{cases}$$

as illustrated in Fig. 8 ($t = 0$ panel) for $x_0 = 190$ and $w = 10$, with $c = 1 = c_0$ and $\varepsilon = 1 \cdot 10^{-4}$. In this case, the dilated compacton with amplitude 1.33 decomposes into three compactons of decreasing amplitudes 1.86, 1.25, and 0.400, values that remain constant from $t = 40$ until $t = 100$. The three compactons are separated by dissipative plateaus and accompanied by an oscillatory tail residual of increasing frequency and decreasing amplitude towards its left side. The panels at $t = 20$, 40, and 60 show that the oscillatory tail separates from the smallest compacton and stretches as time passes. At $t = 80$ the tail has reentered the domain, overlapping with the leading compacton. Finally, at $t = 100$ the tail reaches the right boundary of the second compacton. The bottom left panel shows a contour plot with the three compactons in yellow, green and blue color, and the residual and the oscillatory tail in dark blue. Finally, the bottom right panel shows a surface plot of the solution with the initial condition highlighted in red color.

The numerical adiabatic perturbation fails in order to predict the evolution of the second invariant for the generation of compacton trains from the dilated compacton initial conditions. Fig. 9 compares the second invariant (blue curve in top panels) with its adiabatic prediction (red curve with black circles in top panels) and their corresponding time derivatives (bottom panels); the left panels show the whole time interval $[0, 100]$ and the right ones a zoomed time interval $[0, 5]$. The top and bottom left panels show that the adiabatic prediction follows the same trends as the invariant for $t \in [2, 100]$. In fact, if Eq. (13) is solved by using $I_2(2.5)$ as initial condition instead of $I_2(0)$, the new predicted curve only deviates from the invariant about 0.005% (not illustrated in the figure).

The top right panel in Fig. 9 shows that the adiabatic prediction (red curve with circles) deviates slowly from the second invariant until $t \approx 1$; there it starts a larger deviation up to $t \approx 2$, after which the deviation remains nearly constant; at $t \approx 2$, the relative error is about 0.048%, increasing slowly up to 0.056% at $t = 100$. The bottom right panel shows that the observed deviation is due to fluctuations in the time derivative of the second invariant estimated by the adiabatic prediction between $t = 0.21$ and $t = 2.25$. Apparently, the fluctuations are associated to the large noise in the numerical evaluation of the third-order derivative in the right-hand side of the adiabatic Eq. (16) observed for $t < 3$. It should be noticed that, when the right-hand side of Eq. (16) is evaluated by using either the second-order or the fourth-order derivative instead of the third-order one, cf. Eq. (12), the results are noisier and the deviations are larger.

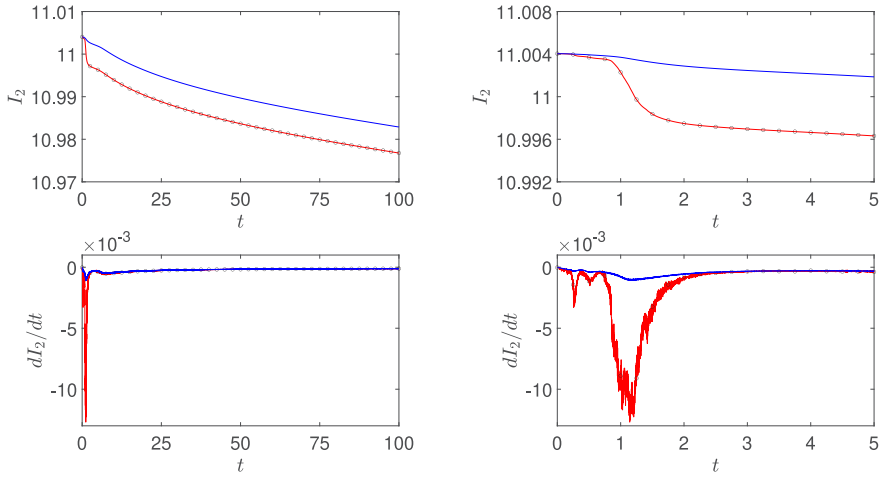

Fig. 9. The evolution of the second invariant (top panels) and its time derivative (bottom panels) for the $|K|(2,2)$ equation (blue line) and the corresponding predictions from adiabatic perturbations (red line with black circles) for the solutions plotted in Fig. 8. (For interpretation of the references to color in this figure legend, the reader is referred to the web version of this article.)

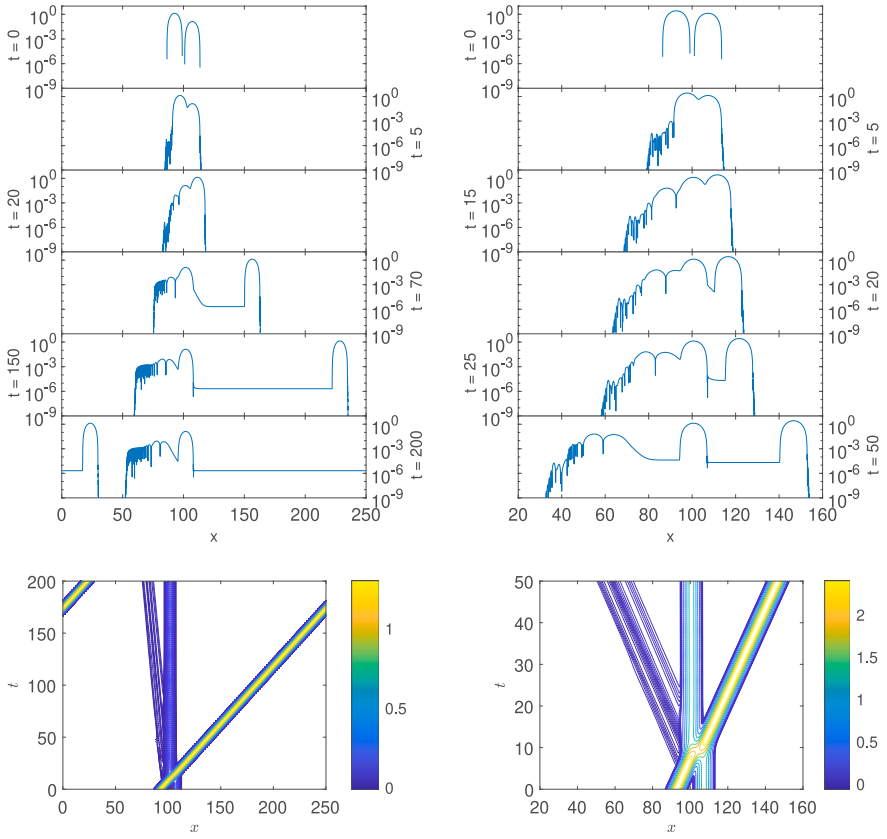

Fig. 10. Compacton–compacton chase collisions for the $|K|(2,2)$ equation with compacton speeds of $c_1 = 1$ and $c_2 = 0.1 = c_0$, and hyperviscosity $\varepsilon = 1 \cdot 10^{-5}$ (left panels), and $c_1 = 2$, $c_2 = 1 = c_0$, and $\varepsilon = 1 \cdot 10^{-4}$ (right panels), both by using $\Delta x = 0.01$, and $\Delta t = 0.002$.

5.4. Compacton–compacton chase collisions

In order to evaluate the effectiveness of the numerical adiabatic perturbation theory for the evolution of the second invariant in compacton–compacton chase collisions, let us start with the $|K|(2,2)$ equation. Fig. 10 (left panels) shows a compacton–compacton

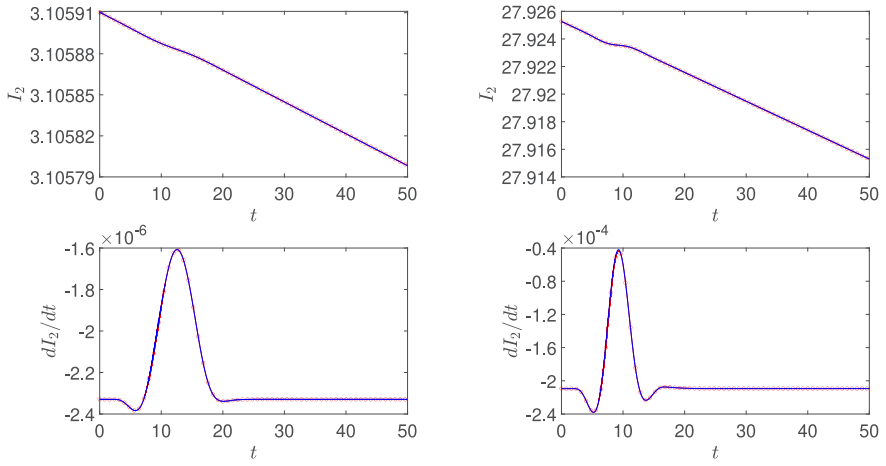

Fig. 11. Evolution of the second invariant (top panels) and its time derivative (bottom panels) for the $|K|(2,2)$ equation (blue line) and the corresponding predictions from adiabatic perturbation (red line with red circles) in compacton–compacton chase collisions with compacton speeds $c_1 = 1$ and $c_2 = 0.1 = c_0$, and hyperviscosity $\varepsilon = 1 \cdot 10^{-5}$ (left panels), and $c_1 = 2$, $c_2 = 1 = c_0$, and $\varepsilon = 1 \cdot 10^{-4}$ (right panels), by using $\Delta x = 0.01$, and $\Delta t = 0.002$. (For interpretation of the references to color in this figure legend, the reader is referred to the web version of this article.)

chase collision with speeds $c_1 = 1$ and $c_2 = 0.1 = c_0$, and $\varepsilon = 1 \cdot 10^{-5}$. The top left panel at $t = 0$ shows the initial condition with both compactons by using a logarithmic vertical scale. At $t = 5$ it shows both compactons during its interaction and the appearance of a backward radiation with a sharp front. At $t = 20$, the tallest compacton has crossed the smallest one, being at its right; additionally, the left part of the zero-mass residual is appearing at left side of the smallest compacton. At $t = 70$, the separation of the tallest compacton from the other one is observed, with a dissipative plateau between them with an amplitude of $2.1 \cdot 10^{-6}$; the residual generates an oscillatory tail with an amplitude larger than that of the backward radiation.

The residual is separating from the smallest compacton at $t = 150$ in the top left panel in Fig. 10, with its oscillatory tail stretching towards the left. Finally, at $t = 200$, the larger compacton has reentered the domain, approaching the oscillatory tail of the residual, that is well-separated from the smallest compacton. The bottom left panel in Fig. 10 shows a contour plot of this solution, with the leading compacton in yellow, the other compacton in blue, and the residual in dark blue (the whole oscillatory tail of the residual is not illustrated for clarity).

Fig. 10 (right panels) shows a compacton–compacton chase collision with speeds $c_1 = 2$ and $c_2 = 1 = c_0$, and $\varepsilon = 1 \cdot 10^{-4}$. At $t = 5$, while the compactons are interacting, a backward radiation with a sharp front is observed. At $t = 15$, the tallest compacton has exchanged its relative position with the smallest one, and simultaneously half of the zero-mass residual has appeared at left side of the smallest compacton; the residual has an amplitude larger than that of the backward radiation visible at its left side. At $t = 20$, both compactons are well separated, with the residual connected to the smallest one, and the backward radiation moving to the left with a speed of $-c_0$.

The dissipative plateau between both compactons is appearing at $t = 25$ in the top right panel in Fig. 10, with the residual and its oscillatory tail propagating towards the left direction. Finally, at $t = 50$, the compactons are separated by a plateau of amplitude $2.1 \cdot 10^{-5}$, with another plateau of $4.2 \cdot 10^{-5}$ between the residual and the smallest compacton; the oscillatory tail of the residual is stretching towards the left, with an amplitude larger than that of the backward radiation. The bottom right panel in Fig. 10 shows a contour plot of the solution, with the leading compacton in yellow, the other compacton in light blue, and the residual and the first part of the oscillatory tail in dark blue.

Fig. 11 shows that the evolution of the second invariant during the compacton–compacton chase collisions for the $|K|(2,2)$ equation shown in Fig. 10 is in an excellent agreement with the prediction of the numerical adiabatic perturbation theory. The top panels show that, before and after the chase collision, the second invariant $I_2(t)$ exponentially decays as predicted by the corresponding equation in Table 1, but during the chase collision the slope of the second invariant changes. During the whole simulation, the prediction of the adiabatic perturbation $I_{2\varepsilon}(t)$ (blue curve) coincides with the evolution of the invariant $I_2(t)$ (red curve with circles).

The agreement is further illustrated in the bottom panels in Fig. 11, that show the evolution in time of dI_2/dt (blue curve) and $dI_{2\varepsilon}/dt$ (red curve with circles). During the compacton–compacton chase collision, both have a small minimum, a big maximum and then another small minimum; after the chase collision both remain constant. Let us emphasize that the panels show the time interval $[0, 50]$ in order to highlight the chase collision, although the excellent agreement continues in the whole time interval of the simulation, $t \in [0, 200]$.

The behavior of the adiabatic perturbation theory for the prediction of the evolution of the second invariant in the compacton–compacton chase collisions can also be illustrated for the $|K|(p,p)$ equation for non-integer $p \neq 2$. Fig. 12 shows contour plots for four representative compacton–compacton chase collision with $p = 1.5$ (top left panel), $p = 2.5$ (top right), $p = 3.5$ (bottom left) and $p = 4.5$ (bottom right panel), all with $c_1 = 1 = c_0$, $c_2 = 0.9$, and $\varepsilon = 1 \cdot 10^{-5}$. In the initial condition, the position of both

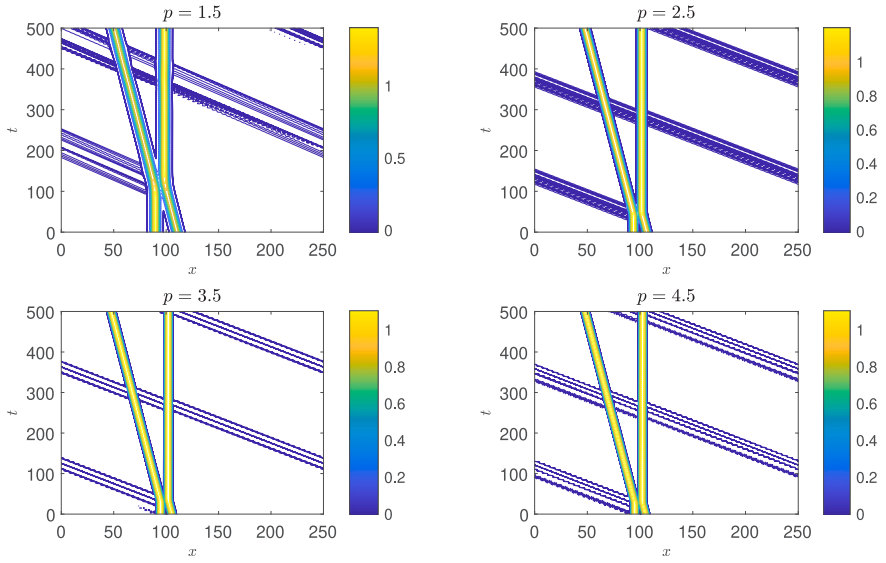

Fig. 12. Contour plots of the compacton–compacton chase collision for the $|K|(p,p)$ equation with $p = 1.5$ (top left panel), $p = 2.5$ (top right panel), $p = 3.5$ (bottom left panel) and $p = 4.5$ (bottom right panel), with $c_1 = 1 = c_0$, $c_2 = 0.9$, $\varepsilon = 1 \cdot 10^{-5}$, $\Delta x = 0.01$, and $\Delta t = 0.002$.

compactons are $x_{0,1} = 99 - w_p/2$ and $x_{0,2} = 101 + w_p/2$, where $w_p = 2\pi p/(p-1)$ is the width of the compacton (3). The four panels show similar trends, although the compactons and the residual are wider for smaller p: the two compactons collide and separate, generating during the interaction a residual moving backwards at $-c_0$ with an oscillatory tail that stretches towards the left (it should be noticed that only the oscillations with higher amplitudes of the tail, which exhibits the lowest frequencies, are the only ones shown plotted in contour plots for clarity). The residual reenters the domain two times, crossing both compactons with a small change in its slope after the interaction with each compacton. However, there is no noticeable change in the slope of the compactons.

Fig. 13 compares the evolution of the second invariant (blue curves) and the prediction of the adiabatic perturbation (red curves with circles) for the $|K|(p,p)$ equation with $p = 1.5$ (top left panels), 2.5 (top right ones), 3.5 (bottom left ones), and 4.5 (bottom right ones). For $p = 1.5$, both curves agree until $t = 380$ where the adiabatic prediction deviates from the second invariant (top part of the $p = 1.5$ panel), due to a large deviation of the time derivative of the second invariant in the adiabatic prediction (bottom part of the $p = 1.5$ panel); note that there is an additional small deviation in the time derivative from $t = 120$, that disappears around $t = 280$, but whose effect on the invariant is not noticeable in the top part of the $p = 1.5$ panel.

The agreement between the adiabatic prediction and the evolution of the invariant and its time derivative is excellent for $p = 2.5$, 3.5, and 4.5 as illustrated in the corresponding panels in Fig. 13. For $p = 2.5$ (top right panels), the behavior is very similar to that observed for $p = 2$ on the left panels in Fig. 11. However, for $p = 3.5$ (bottom left panels), the invariant increases in time, as expected from the propagation one compacton with $p > (3 + \sqrt{13})/2 \approx 3.303$ (see the discussion of Table 1 in the main text). However, during the compacton–compacton chase collision, the slope of the second invariant temporally changes its sign (top part of the $p = 3.5$ panel), as observed in its time derivative (bottom part of the $p = 3.5$ panel), which is matched accurately by the adiabatic perturbation. Finally, for $p = 4.5$ (bottom right panels), the slope of the second invariant decreases during the chase collision (top part of the $p = 4.5$ panel), but without changing sign, as illustrated by its time derivative (bottom part of the $p = 4.5$ panel).

The second invariant for compacton–compacton chase collisions of the $K(p,p)$ equation decreases before and after the chase collision for $p = 2.5$, but increases in both cases for $p = 3.5$; the value of p at which this change in the slope occurs can be numerically estimated as follows. For such a task, the slopes of $I_2(t)$ and $I_{2\varepsilon}(t)$ can be calculated by linear fitting its values after the chase collision, i.e., in the interval $t \in [55, 100]$. In Section 5.1, for one compacton, it has been shown that the change in slope occurs for $p = 3.3318$; we expect a similar value for the compacton–compacton chase collision. However, the slopes are $-5.99 \cdot 10^{-7}$ and $-7.68 \cdot 10^{-8}$ for $p = 3.31$ and 3.32, respectively.

Fig. 14 shows the evolution of I_2 (blue curve) and of $I_{2\varepsilon}$ (red curve with circles) during the chase collision for $p = 3.32$ (top left panel), 3.33 (top right panel), 3.34 (bottom left panel), and 3.35 (bottom right panel). The slope of the invariant for $t \in [55, 100]$ is negative for $p = 3.32$ and $p = 3.33$, being in the last case $-1.40 \cdot 10^{-8}$. However, for $p = 3.34$ and 3.35, the slope becomes positive, specifically, $4.92 \cdot 10^{-8}$ and $1.13 \cdot 10^{-7}$, respectively. Although not illustrated in the plots, the slope change occurs between $p = 3.332222$ and 3.332224, for which the slopes are $-5.80 \cdot 10^{-12}$ and $7.54 \cdot 10^{-12}$, respectively; in fact, for $p = 3.332223$ the slope is $-2.13 \cdot 10^{-13}$, being zero in practice (the invariant oscillates irregularly around a constant value in the time interval $t \in [55, 100]$). The critical value of p for this change in slope can be estimated by using a linear interpolation, resulting in $p = 3.3322229 \pm 0.0000001$.

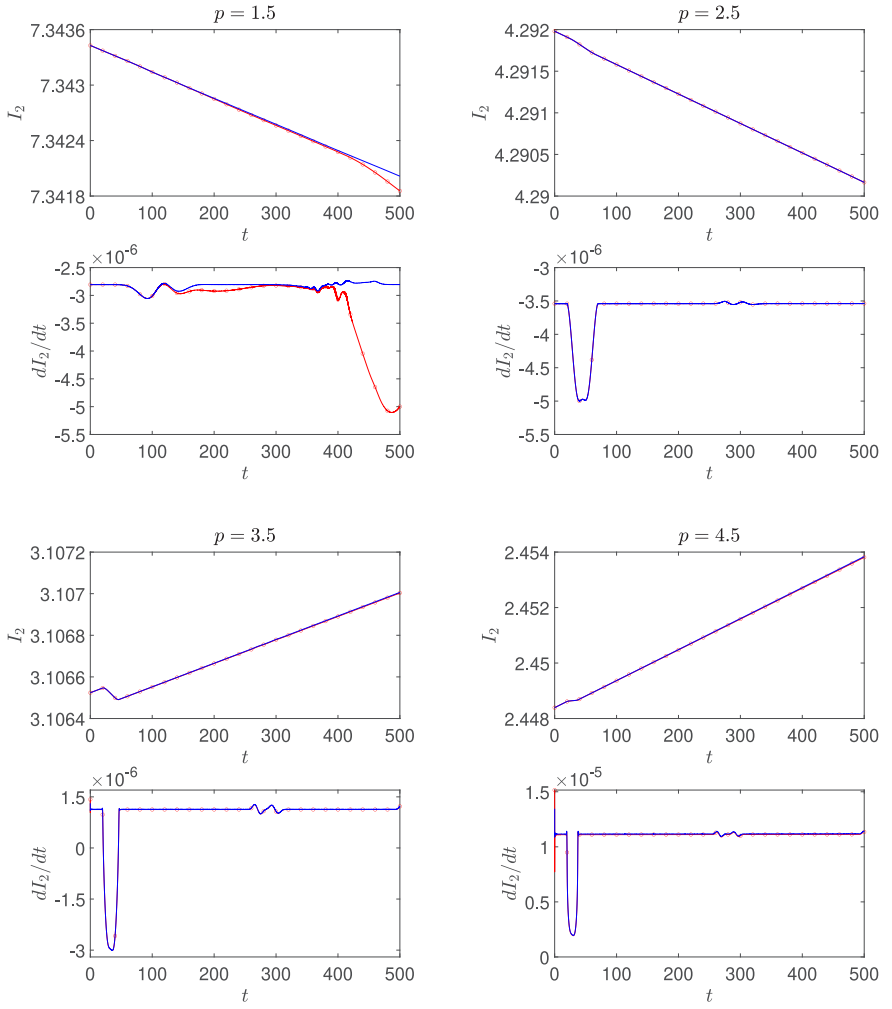

Fig. 13. Evolution of the second invariant (I_2) and its time derivative (dI_2/dt) for the $|K|(p,p)$ equation (blue line) and the corresponding predictions from adiabatic perturbation (red line with red circles) in compacton–compacton chase collisions for $p = 1.5$ (top left panels), $p = 2.5$ (top right panels), $p = 3.5$ (lower left panels) and $p = 4.5$ (lower right panels) with compacton speeds $c1 = 1 = c_0$ and $c_2 = 0.9$, and hyperviscosity $\varepsilon = 1 \cdot 10^{-5}$ by using $\Delta x = 0.01$, and $\Delta t = 0.002$. (For interpretation of the references to color in this figure legend, the reader is referred to the web version of this article.)

5.5. Compacton–anticompacton chase collisions

The adiabatic perturbation theory for the evolution of the second invariant can also be evaluated in compacton–anticompacton chase collisions for the $|K|(p,p)$ equation. Fig. 15 shows contour plots for chase collisions with $p = 1.5$ (top left panel), $p = 2.5$ (top right), $p = 3.5$ (bottom left) and $p = 4.5$ (bottom right); in the initial condition, the compacton has speed $c_1 = 1 = c_0$ and is located at $x_{0,1} = 99 - w_p/2$, and the anticompacton has speed $c_2 = -0.5$ and is located at $x_{0,2} = 101 + w_p/2$. In the contour plots, the compactons have yellow color, the anticompactons have dark blue color, and the residual has either blue or cyan color; note that compactons and anticompactons are wider for smaller p.

The four panels in in Fig. 15 show similar trends. The compacton and the anticompacton collide and separate, generating a residual that moves backwards at about $-c_0$ with an oscillatory tail that stretches towards the left (in the contours only the first oscillations of this tail are plotted for clarity). The residual reenters the domain two times, crossing both compactons with a change in its slope after the interaction with each compacton; but there is no noticeable change in the slope of the compactons. Let us highlight that, for $p > 1.5$, a second chase collision between the compacton and the anticompacton is observed around $t = 500$.

Fig. 16 compares the prediction of the adiabatic perturbation theory and the evolution of the second invariant in the compacton–anticompacton chase collisions for the $|K|(p,p)$ equation with $p = 1.5$, 2.5, 3.5, and 4.5, and hyperviscosity $\varepsilon = 1 \cdot 10^{-4}$ (the same simulations shown in Fig. 15). For $p = 1.5$ (top left panels), the prediction $I_{2\varepsilon}$ (red curve with black circles) only agrees with the invariant I_2 (blue curve) before the start of the chase collision at $t = 17$; after this time, a large deviation is observed, with a final relative error of 4.4% at $t = 500$. This mismatch is due to the large deviation between dI_2/dt (blue curve) and $dI_{2\varepsilon}/dt$ (red curve

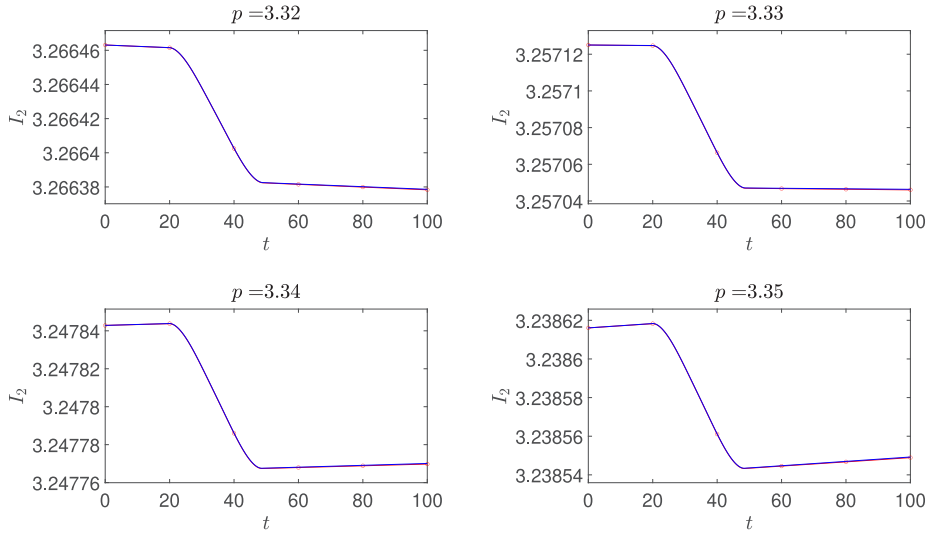

Fig. 14. Simulation of a chase collision compacton–compacton for the $|K|(p,p)$ equation with $p = 3.32$ (top left panel), 3.33 (top right panel), 3.34 (bottom left panel), and 3.35 (bottom right panel), in the comoving frame of reference of the first compacton, with speeds $c_1 = 1 = c_0$ and $c_2 = 0.9$, by using $\Delta x = 0.01$, $\Delta t = 0.002$, $\varepsilon = 1 \cdot 10^{-5}$, and $t \in [0, 100]$.

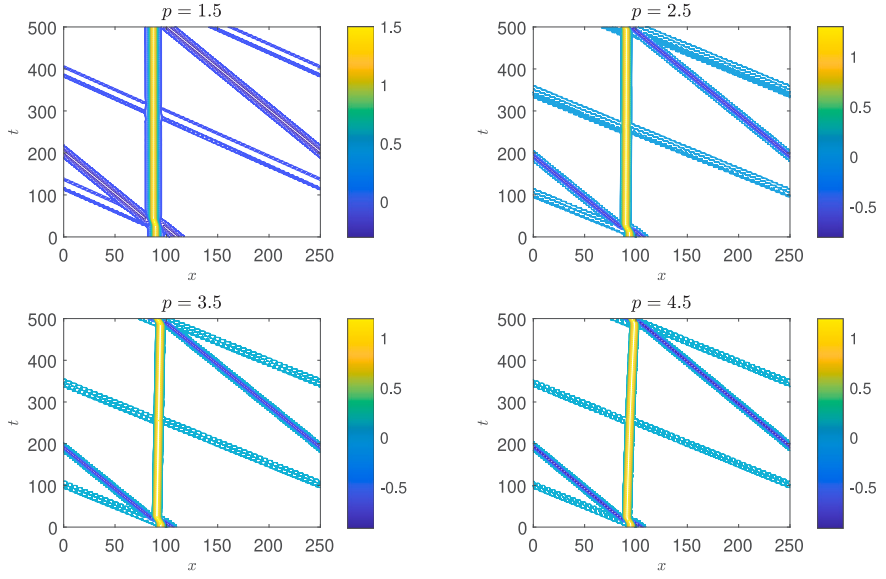

Fig. 15. Contour plots of the compacton–anticompacton chase collision for the $|K|(p,p)$ equation with $p = 1.5$ (top left panel), $p = 2.5$ (top right panel), $p = 3.5$ (bottom left panel) and $p = 4.5$ (bottom right panel), with $c_1 = 1 = c_0$, $c_2 = -0.5$, $\varepsilon = 1 \cdot 10^{-4}$, $\Delta x = 0.01$, and $\Delta t = 0.002$.

with circles) shown in the bottom part of the $p = 1.5$ panel; although dI_2/dt remains nearly constant, $dI_{2\varepsilon}/dt$ shows a change of two orders of magnitude with a minimum about $t \approx 50$.

The plot insert in the bottom part of the $p = 1.5$ panel in Fig. 16 shows that dI_2/dt (blue curve) has a V-like shape between $t = 17$ and 60; specifically, it increases up to a small maximum, then decreases down to a large minimum, increases again up to a maximum similar to the previous one, and, finally, returns to its original value. The profile of the change in $dI_{2\varepsilon}/dt$ (red curve) in the bottom part of the $p = 1.5$ panel is not related with this V-like shape, being asymmetrical, with large gradients before reaching a minimum and with a subsequent exponential relaxation towards the dI_2/dt curve. We expect that during a future second chase collision a new large deviation will appear in $dI_{2\varepsilon}/dt$ (not observed in the plot).

For $p = 2.5$ (top right panels in Fig. 16), the invariant I_2 (blue curve) has a behavior similar to that observed for $p = 1.5$, with a large deviation of the adiabatic prediction $I_{2\varepsilon}$ (red curve with circles) after the chase collision, with a final error of 3.8% at $t = 500$. However, dI_2/dt (bottom part of the $p = 2.5$ panel) shows a local maximum, instead of the V-like shape observed for $p = 1.5$. The prediction $dI_{2\varepsilon}/dt$ shows large oscillations during the chase collision. The reason could be the large gradients of the solution during

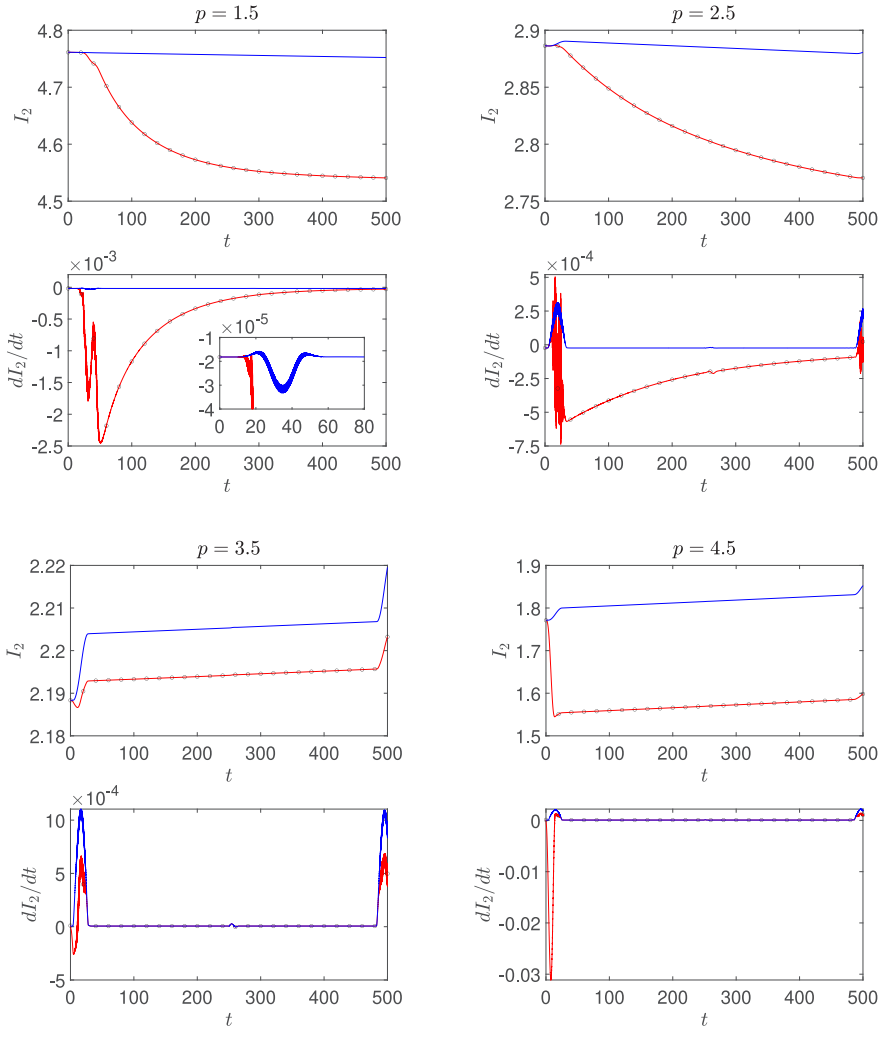

Fig. 16. Evolution of the second invariant (I_2) and its time derivative (dI_2/dt) for the $|K|(p,p)$ equation (blue line) and the corresponding predictions from adiabatic perturbation (red line with red circles) in compacton–anticompacton chase collisions for $p = 1.5$ (top left panels), $p = 2.5$ (top right panels), $p = 3.5$ (lower left panels) and $p = 4.5$ (lower right panels) with compacton speeds $c1 = 1 = c_0$ and $c_2 = 0.5$, and hyperviscosity $\epsilon = 1 \cdot 10^{-4}$ by using $\Delta x = 0.01$, and $\Delta t = 0.002$. (For interpretation of the references to color in this figure legend, the reader is referred to the web version of this article.)

the chase collisions that result in large errors in the numerical approximation of its third-order derivative in the right-hand side of the adiabatic Eq. (16); like in the case of the dilated compacton presented in Section 5.3.

The adiabatic perturbation theory prediction for the time derivative of the second invariant is in good agreement with the numerical result between compacton–anticompacton chase collisions for the $|K|(p,p)$ equation with $p > 3$, however, during the chase collisions there are deviations that result in a constant mismatch between this invariant and its adiabatic prediction. This behavior is illustrated in Fig. 16, for $p = 3.5$ (bottom left panels), where the I_2 (blue curve) grows in time, but with a large change in slope during the two chase collisions occurring in $t \in [0, 500]$. The value of dI_2/dt (blue curve) in the bottom $p = 3.5$ panel is always positive, with a local maximum during the chase collisions; however, that of $dI_{2\epsilon}/dt$ (red curve with black circles) has a negative minimum for $t < 10.5$, and a subsequent positive maximum, smaller than that of dI_2/dt, during the first chase collision; between the chase collisions, it follows the same trend as dI_2/dt. It should be noticed that, during the second chase collision, only the local positive maximum in $dI_{2\epsilon}/dt$ is observed, which is also smaller than that of dI_2/dt. Quantitatively, after the first chase collision, the deviation between I_2 and $I_{2\epsilon}$ is about 0.5%, remaining nearly constant until the second chase collision; the final deviation, during the second chase collision, is of 0.7% at $t = 500$.

For $p = 4.5$ (bottom right panels), the invariant I_2 (blue curve) grows in time, with changes in slope during the chase collisions; in general trends, the behavior is similar to that observed for $p = 3.5$. The adiabatic prediction $dI_{2\epsilon}/dt$ (red curve with black circles in the bottom part of the $p = 4.5$ panel) is negative in the time derivative for $t < 13.8$, with a large local minimum (two orders of magnitude larger than the one observed for $p = 3.5$); subsequently, a local positive maximum is observed, but smaller than that of dI_2/dt. After the first chase collision, there is a good agreement between dI_2/dt and $dI_{2\epsilon}/dt$; however, there is a constant deviation

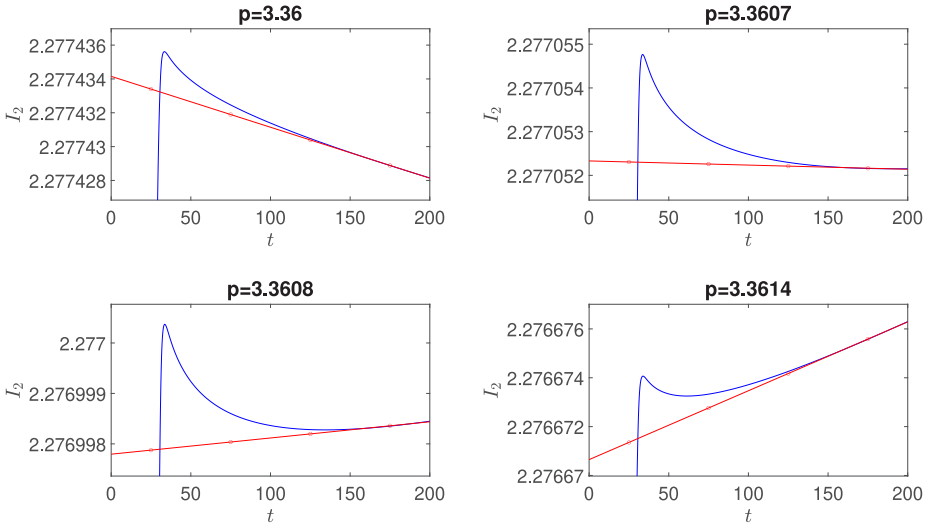

Fig. 17. The evolution in time of the second invariant (blue curve) and its linear fit in $t \in [150, 200]$ (red curve with circles) in a compacton–anticompacton chase collision for the $|K|(p,p)$ equation with $p = 3.3600$ (top left panel), 3.3607 (top right panel), 3.3608 (bottom left panel), and 3.3614 (bottom right panel), with speeds $c_1 = 1 = c_0$ and $c_2 = 0.9$, by using $\Delta x = 0.01$, $\Delta t = 0.002$, $\epsilon = 1 \cdot 10^{-5}$, $x \in [0, 250]$, and $t \in [0, 200]$. (For interpretation of the references to color in this figure legend, the reader is referred to the web version of this article.)

of about 13.6% between the invariant I_2 and its prediction $I_{2\epsilon}$ (top chase $p = 4.5$ panel); the final deviation is 13.7% at $t = 500$ (during the second chase collision).

The second invariant after the compacton–anticompacton chase collision for the $|K|(p,p)$ equation has a negative slope for $p = 1.5$ and 2.5, but a positive one for $p = 3.5$ and 4.5 as shown in Fig. 16. Hence, there is a critical value of p where this change in the slope occurs, that can be determined by using linear interpolation of the slopes. Fig. 17 illustrates the evolution of the second invariant for $t \in [0, 200]$ (blue curve) and its linear fit in $t \in [150, 200]$ (red curve with circles) in a compacton–anticompacton chase collision for the $|K|(p,p)$ equation with $p = 3.36$ (top left panel), 3.3607 (top right panel), 3.3608 (bottom left panel), and 3.3614 (bottom right panel). For $p = 3.3600$ and 3.3607 the slopes of $I_2(t)$ in $t \in [150, 200]$ are negative, $-3.01 \cdot 10^{-8}$ and $-9.51 \cdot 10^{-10}$, respectively, but for $p = 3.3608$ and 3.3614 they are positive, $3.21 \cdot 10^{-9}$ and $2.82 \cdot 10^{-8}$, resp.; in all these cases the slope for $I_{2\epsilon}$ is positive (although not illustrated in the plots because its values are outside their vertical axis span). A linear fit estimates that the critical value of p is given by 3.3607228 ± 0.0000001.

6. Conclusions

The adiabatic perturbation theory has been applied to the $|K|(p,p)$ equation numerically solved by a Petrov–Galerkin method with small hyperviscosity. This numerical method exactly preserves the first invariant, but does not conserve the second invariant, which evolves in time as a function of the hyperviscosity parameter. For the propagation of a single compacton, this theory predicts that the compacton speed is a function of a slow time scale governed by an ordinary differential equation; its analytical solution has been obtained. It determines the adiabatic evolution of the second invariant, which decreases or increases depending on whether p is smaller or larger than a critical value $p_{cr} = (3 + \sqrt{13})/2 \approx 3.303$.

We have observed that the numerical propagation of a single compacton of the $|K|(2,2)$ equation without hyperviscosity presents an instability associated with the CFL condition. The compacton emits thin wavepackets of radiation with a group velocity larger than that of the compacton and those of the fronts of the numerically-induced, forward and backward radiation. The CFL condition should cope with such thin wavepackets in order to avoid potential instabilities in simulations without hyperviscosity. It should be highlighted that such instabilities do not appear when small hyperviscosity is included in the simulation.

The evolution of the second invariant during the numerical propagation of a single compacton of the $|K|(p,p)$ equation with small hyperviscosity agree with the predictions of the numerical adiabatic perturbation theory. However, there is a small discrepancy in the estimation of the critical value of p that separates when the evolution of the second invariant either decreases or increases as a function of the hyperviscosity. The numerical estimation yields a critical value of $p \approx 3.332$, which differs from the analytical value $p_{cr} \approx 3.303$. This small difference of about 1% could be associated with the emission of the numerically-induced radiation.

A numerical implementation of the adiabatic perturbation has been developed for solutions of the $|K|(p,p)$ equation with multiple compactons simulated with small hyperviscosity. The numerical adiabatic prediction is in excellent agreement with the numerical evolution of the invariant in the propagation of a single compacton, the generation of compacton trains from a truncated cosine initial condition, and compacton–compacton chase collisions. However, there is a discrepancy between the adiabatic prediction and the numerical results for scenarios involving the generation of a compacton train from a dilated compacton and compacton–anticompacton chase collisions. While there is an initial agreement, substantial deviations in the invariant evolution with respect

to the adiabatic prediction are observed when the solution have large spatial gradients. Currently, we have no explanation for such a discrepancy.

The numerical estimation of the critical value of p in compacton–compacton chase collisions result in a value ≈ 3.332; this value coincides with the one obtained for the propagation of a single compacton, reinforcing the agreement of the numerical adiabatic prediction of the second invariant. However, in the case of compacton–anticompacton chase collisions, a critical $p \approx 3.360$ is estimated. The origin of this discrepancy with the result for compacton–compacton chase collisions may be related with the disagreement between the numerical adiabatic predictions and the evolution of the second invariant in such cases.

Let us summarize some lines for further research. In general terms, our findings validate the use of the adiabatic perturbation theory for the analysis of the numerically-induced evolution of the invariants due to the hyperviscosity. Hence, they suggest that modifying the numerical method to correct for the effects introduced by the hyperviscosity could lead to a new numerical scheme that nearly preserves the second invariant. Our intention is to study it in the near future.

Additionally, we have observed wavepackets of numerically-induced radiation generated from the one compacton solution in numerical simulations conducted without hyperviscosity. Their detailed analysis, by using a slowly varying envelope approximation and proper perturbation methods, is also an interesting topic for further research.

Finally, we have studied a numerical method for the $|K|(p,p)$ equation; in the future we will evaluate the adiabatic perturbation theory with alternative numerical methods to determine whether it also predicts the corresponding numerically-induced phenomena with similar success.

CRediT authorship contribution statement

Rubén Garralon-López: Methodology, Software, Writing – original draft, Writing – reviewing & editing. **Francisco Rus:** Conceptualization, Methodology, Software, Writing – original draft, Writing – reviewing & editing, Supervision. **Francisco R. Villatoro:** Conceptualization, Writing – original draft, Writing – reviewing & editing, Supervision, Project administration, Funding acquisition.

Acknowledgments

We thank the three reviewers for their helpful comments that have improved the presentation of the contents of this paper. The research reported here was partially supported by Project RoCoSoyCo (UMA18-FEDERJA-248) of the Consejería de Economía y Conocimiento, Junta de Andalucía, Spain. Funding for open access charge: Universidad de Málaga / CBUA.

References

[1] M.J. Ablowitz, S.D. Nixon, T.P. Horikis, D.J. Frantzeskakis, Perturbations of dark solitons, Proc. R. Soc. A-Math. Phys. Eng. Sci. 467 (2133) (2011) 2597–2621.
[2] M. Ahmat, J. Qiu, Direct WENO scheme for dispersion-type equations, Math. Comput. Simulation 204 (2023) 216–229.
[3] M. Antonova, A. Biswas, Adiabatic parameter dynamics of perturbed solitary waves, Commun. Nonlinear Sci. Numer. Simul. 14 (3) (2009) 734–748.
[4] A. Cardenas, B. Mihaila, F. Cooper, A. Saxena, Properties of compacton-anticompacton collisions, Phys. Rev. E 83 (6) (2011) 066705, http://dx.doi.org/10.1103/PhysRevE.83.066705.
[5] Y. Chen, J. Yan, X. Zhong, Cell-average based neural network method for third order and fifth order KdV type equations, Front. Appl. Math. Stat. 8 (2022) 1021069.
[6] A. Chertock, D. Levy, Particle methods for dispersive equations, J. Comput. Phys. 171 (2) (2001) 708–730.
[7] J. DeFrutos, M.A. Lopez-Marcos, J.M. Sanz-Serna, A finite difference scheme for the $K(2,2)$ compacton equation, J. Comput. Phys. 120 (2) (1995) 248–252.
[8] J.-C. Fernandez, C. Froeschle, G. Reinisch, Adiabatic perturbations of solitons and shock waves, Phys. Scr. 20 (3–4) (1979) 545–551.
[9] V.A. Galaktionov, S.R. Svirshchevskii, Exact Solutions and Invariant Subspaces of Nonlinear Partial Differential Equations in Mechanics and Physics, Chapman and Hall/CRC, New York, 2006.
[10] J. Garralón, F. Rus, F.R. Villatoro, Compacton numerically-induced radiation in a fourth-order finite element method, WSEAS Trans. Math. 5 (1) (2006) 89–96.
[11] J. Garralón, F. Rus, F.R. Villatoro, Removing trailing tails and delays induced by artificial dissipation in Padé numerical schemes for stable compacton collisions, Appl. Math. Comput. 220 (2013) 185–192.
[12] J. Garralón, F.R. Villatoro, Dissipative perturbations for the $K(n,n)$ Rosenau–Hyman equation, 17 (12) (2012) 4642–4648.
[13] R. Garralón-López, F. Rus, F.R. Villatoro, Compacton-anticompacton collisions in the Rosenau–Hyman $K(p,p)$ equation by numerical simulations with hyperviscosity, Commun. Nonlinear Sci. Numer. Simul. 117 (2023) 106927.
[14] R. Garralón-López, F. Rus, F.R. Villatoro, Robustness of the absolute Rosenau–Hyman $|K|(p,p)$ equation with non-integer p, Chaos Solitons Fractals 169 (2023) 113216.
[15] L. Girgis, A. Biswas, Soliton perturbation theory for nonlinear wave equations, Appl. Math. Comput. 216 (7) (2010) 2226–2231.
[16] R. Grimshaw, E. Pelinovsky, T. Talipova, Damping of large-amplitude solitary waves, Wave Motion 37 (4) (2003) 351–364.
[17] R. Herman, C. Knickerbocker, Numerically induced phase shift in the KdV soliton, J. Comput. Phys. 104 (1) (1993) 50–55.
[18] T.T. Huynh, Q.M. Nguyen, Fast soliton interactions in cubic-quintic nonlinear media with weak dissipation, Appl. Math. Model. 97 (2021) 650–665.
[19] M.S. Ismail, T.R. Taha, A numerical study of compactons, Math. Comput. Simulation 47 (6) (1998) 519–530.
[20] A. Karczewska, P. Rozmej, E. Infeld, G. Rowlands, Adiabatic invariants of the extended KdV equation, Phys. Lett. A 381 (4) (2017) 270–275.
[21] Y.S. Kivshar, B.A. Malomed, Dynamics of solitons in nearly integrable systems, Rev. Modern Phys. 61 (1989) 763–915, http://dx.doi.org/10.1103/RevModPhys.61.763.
[22] S. Kumbinarasaiah, W. Adel, Hermite wavelet method for solving nonlinear Rosenau–Hyman equation, Partial. Differ. Equ. Appl. Math. 4 (2021) 100062.
[23] B. Mihaila, A. Cardenas, F. Cooper, A. Saxena, Stability and dynamical properties of Rosenau–Hyman compactons using Padé approximants, Phys. Rev. E 81 (5) (2010) 056708.
[24] A.A. Nkongho, A.M. Dikandé, C.R.F. Mbobda, Solitary-wave dynamics in an R^2LC nonlinear transmission line with voltage bias, Results Phys. 35 (2022) 105303.

[25] M. Obregon, N. Raj, Y. Stepanyants, Adiabatic decay of internal solitons due to Earth's rotation within the framework of the Gardner–Ostrovsky equation, Chaos 28 (3) (2018) 033106, http://dx.doi.org/10.1063/1.5021864.
[26] D.E. Pelinovsky, A.V. Slunyaev, A.V. Kokorina, E.N. Pelinovsky, Stability and interaction of compactons in the sublinear KdV equation, Commun. Nonlinear Sci. Numer. Simul. 101 (2021) 105855.
[27] S.P. Popov, New compacton solutions of an extended Rosenau–Pikovsky equation, Comput. Math. Math. Phys. 57 (2017) 1540–1549.
[28] S.P. Popov, Compactons and Riemann waves of an extended modified Korteweg–de Vries equation with nonlinear dispersion, Comput. Math. Math. Phys. 58 (2018) 437–448.
[29] S.P. Popov, Compacton solutions of the Korteweg–de Vries equation with constrained nonlinear dispersion, Comput. Math. Math. Phys. 59 (2019) 150–159.
[30] P. Rosenau, On a class of nonlinear dispersive-dissipative interactions, Physica D 123 (1–4) (1998) 525–546.
[31] P. Rosenau, J. Hyman, Compactons: Solitons with finite wavelength, Phys. Rev. Lett. 70 (5) (1993) 564–567, http://dx.doi.org/10.1103/PhysRevLett.70.564.
[32] P. Rosenau, A. Zilburg, Compactons, J. Phys. A 51 (34) (2018) 343001.
[33] F. Rus, F.R. Villatoro, Padé numerical method for the Rosenau–Hyman compacton equation, Math. Comput. Simul. 76 (1–3) (2007) 188–192.
[34] F. Rus, F.R. Villatoro, Self-similar radiation from numerical Rosenau–Hyman compactons, J. Comput. Phys. 227 (1) (2007) 440–454.
[35] F. Rus, F.R. Villatoro, Numerical methods based on modified equations for nonlinear evolution equations with compactons, Appl. Math. Comput. 204 (1) (2008) 416–422.
[36] F. Rus, F.R. Villatoro, Adiabatic perturbations for compactons under dissipation and numerically-induced dissipation, J. Comput. Phys. 228 (2009) 4291–4302.
[37] A. Slunyaev, A. Kokorina, E. Pelinovsky, Alexey Slunyaev and Anna Kokorina and Efim Pelinovsky, Commun. Nonlinear Sci. Numer. Simul. 127 (2023) 107527.
[38] M. Spiegelman, Flow in deformable porous media. Part 1 Simple analysis, J. Fluid Mech. 247 (1993) 17–38, http://dx.doi.org/10.1017/S0022112093000369.
[39] D. Tan, J. Zhou, X. Wang, Z. Wang, Combined effects of topography and bottom friction on shoaling internal solitary waves in the South China Sea, Appl. Math. Mech. 40 (2019) 421–434.
[40] L.N. Trefethen, J.A.C. Weideman, The exponentially convergent trapezoidal rule, SIAM Rev. 56 (2014) 385–458.
[41] F.R. Villatoro, J.I. Ramos, On the method of modified equations. I: Asymptotic analysis of the Euler forward difference method, Appl. Math. Comput. 103 (2–3) (1999) 111–139.
[42] Y. Wong, T. Keller, A unified numerical model for two-phase porous, mush and suspension flow dynamics in magmatic systems, Geophys. J. Int. 233 (2023) 769–795.
[43] A. Zilburg, P. Rosenau, Loss of regularity in the $K(m,n)$ equations, Nonlinearity 31 (6) (2018) 2651–2665.